Monthly Notices
of the
ROYAL ASTRONOMICAL SOCIETY

MNRAS **457,** 3611–3628 (2016) doi:10.1093/mnras/stw222
Advance Access publication 2016 January 27

Synthetic photometry for M and K giants and stellar evolution: hydrostatic dust-free model atmospheres and chemical abundances

B. Aringer,[1,2]★ L. Girardi,[2] W. Nowotny,[3] P. Marigo[1] and A. Bressan[2,4]

[1]*Dipartimento di Fisica e Astronomia Galileo Galilei, Università di Padova, Vicolo dell'Osservatorio 3, I-35122 Padova, Italy*
[2]*Osservatorio Astronomico di Padova – INAF, Vicolo dell'Osservatorio 5, I-35122 Padova, Italy*
[3]*Department of Astrophysics, University of Vienna, Türkenschanzstraße 17, A-1180 Wien, Austria*
[4]*SISSA, via Bonomea 265, I-34136 Trieste, Italy*

Accepted 2016 January 25. Received 2016 January 24; in original form 2015 October 26

ABSTRACT

Based on a grid of hydrostatic spherical COMARCS models for cool stars, we have calculated observable properties of these objects, which will be mainly used in combination with stellar evolution tracks and population synthesis tools. The high-resolution opacity sampling and low-resolution convolved spectra as well as bolometric corrections for a large number of filter systems are made electronically available. We exploit those data to study the effect of mass, C/O ratio and nitrogen abundance on the photometry of K and M giants. Depending on effective temperature, surface gravity and the chosen wavelength ranges, variations of the investigated parameters cause very weak to moderate and, in the case of C/O values close to 1, even strong shifts of the colours. For the usage with stellar evolution calculations, they will be treated as correction factors applied to the results of an interpolation in the main quantities. When we compare the synthetic photometry to observed relations and to data from the Galactic bulge, we find in general a good agreement. Deviations appear for the coolest giants showing pulsations, mass-loss and dust shells, which cannot be described by hydrostatic models.

Key words: molecular data – stars: AGB and post-AGB – stars: atmospheres – stars: evolution – Hertzsprung–Russell and colour–magnitude diagrams – stars: late-type.

1 INTRODUCTION

As more infrared facilities allowing photometric measurements of faint sources become available, stellar populations in close galaxies are being increasingly observed in the corresponding passbands. Our direct neighbours, the Magellanic Clouds, have their evolved red stars almost completely sampled by surveys such as 2MASS (Skrutskie et al. 2006), IRSF (Kato et al. 2007) and VMC (Cioni et al. 2011) in the near-infrared and by SAGE (Meixner et al. 2006), S^{3}MC (Bolatto et al. 2007), AKARI IRC (Ita et al. 2008) and *WISE* (Nikutta et al. 2014) in the mid-infrared. There are also data for M31 and a few dozens of other galaxies in our vicinity. They have been partially covered by high-resolution near-infrared imaging from the *Hubble Space Telescope* (Dalcanton et al. 2012a,b). The amount of available photometry for distant stellar populations will increase a lot, when new space telescopes like James Webb Space Telescope or Wide-Field Infrared Survey Telescope start to operate.

For the more massive galaxies observed in the infrared, a large fraction of the detected bright point sources are cool M stars with very red colours. In general, these objects are situated in the Hertzsprung–Russell diagram (HRD) on the asymptotic giant branch (AGB), in the region of red supergiants (RSG) and in metal-rich environments often close to the tip of the red giant branch (RGB). They may be confused with carbon stars, if only broad-band photometry is available (Boyer et al. 2013). In order to study their behaviour in colour–colour and colour–magnitude diagrams of galaxies, one needs spectral libraries to convert stellar isochrones into the corresponding observable properties. These should cover the relevant ranges in effective temperature, surface gravity and chemical composition.

Libraries of synthetic spectra have the advantage that they may cover a wide range of well-defined stellar parameters. There are several grids of hydrostatic models, which can be or could be used to study K and M giants. Due to the low temperatures of these objects, the opacities caused by many molecular and atomic lines dominate the atmospheres. Examples are the work of Bessell et al. (1989), Fluks et al. (1994) and Levesque et al. (2005) or large libraries based on the MARCS (Gustafsson et al. 2008) and the PHOENIX codes (Allard, Homeier & Freytag 2012; Husser et al. 2013). For warmer stars, one may also take the spectra from Castelli & Kurucz (2003). All of those models cover different values of the effective

★ E-mail: bernhard.aringer@oapd.inaf.it

temperature, surface gravity, [Fe/H] and in some cases even [α/H]. Results obtained with modified abundances of C, N and O typical for RSG objects were published by Lançon et al. (2007).

In a considerable number of cases, hydrostatic models were also used to generate tables containing synthetic visual and near-infrared photometry for cool oxygen-rich giants as a function of stellar parameters. Examples are the works of Gustafsson & Bell (1979), Bell & Gustafsson (1989), Plez, Brett & Nordlund (1992), Bessell, Castelli & Plez (1998), Houdashelt et al. (2000), VandenBerg & Clem (2003) and Clem et al. (2004). The results of Worthey & Lee (2011) are partly based on observations.

The mentioned hydrostatic models cannot include deviations from spherical symmetry or dynamical processes like pulsation creating shock waves, and mass-loss with dust formation, which become important in the cooler AGB and RSG objects. A grid for M-type AGB variables covering a limited parameter range was produced by Bladh et al. (2015). Because of possible uncertainties of the models, they may be complemented with empirical spectral libraries like the ones from Fluks et al. (1994), Lançon & Wood (2000) and Rayner, Cushing & Vacca (2009, IRTF).

In this work, we discuss a grid of hydrostatic COMARCS models for cool stars, which was mainly designed to provide libraries of synthetic spectra and photometry usable in combination with the PARSEC (Bressan et al. 2012) and COLIBRI (Marigo et al. 2013) evolutionary codes to obtain observable properties of stellar populations. In addition to the primary parameters effective temperature, surface gravity, mass and metallicity, we have also varied the abundances of elements like carbon or nitrogen to take the impact of dredge-up processes into account. This includes new improved calculations for C-type giants, which replace to an ever-increasing extent the data published by Aringer et al. (2009), but are not reviewed here. In the current text, we focus on K and M stars. We first describe the models together with their synthetic spectra and photometry in Section 2. Then we discuss in Section 3 the influence of C/O ratio, nitrogen abundance, mass and the used water opacity on the atmospheric structures and energy distributions as well as on various colour indices. In Section 4, the predicted photometric properties are compared to observed relations and to stars in the Galactic bulge. Moreover, the application of the COMARCS data in combination with isochrones is reviewed. The appendix contains a table with the abundance sets, which are at the moment available in the grid.

2 MODEL ATMOSPHERES AND SYNTHETIC SPECTRA

2.1 Opacities and hydrostatic models

In order to study the spectra and photometric properties of K and M giants, we used hydrostatic model atmospheres computed with the COMARCS program. The latter is based on the version of the MARCS code (Gustafsson et al. 1975, 2008) described in Jørgensen, Johnson & Nordlund (1992) and Aringer, Jørgensen & Langhoff (1997). The models are calculated assuming spherical symmetry and local thermodynamic and chemical equilibrium (LTE). The continuous and atomic or molecular absorption at the frequencies used for the opacity sampling in our calculations is taken from external tables generated with the COMA (Copenhagen Opacities for Model Atmospheres) program. The formation of dust is not included. The current approach is identical to the one described in Aringer et al. (2009) for a grid of carbon star models. For further details, we refer to this work.

The COMA program is an opacity generation code that was originally developed by Aringer (2000) to compute wavelength-dependent absorption coefficients for cool model atmospheres. It has also been used to determine weighted mean opacities for stellar evolution calculations (Cristallo et al. 2007; Lederer & Aringer 2009). In combination with an attached radiative transfer module, COMA was applied in a considerable number of investigations to obtain synthetic photometry and spectra at very different resolution (e.g. Aringer et al. 2009; Nowotny, Höfner & Aringer 2010; Eriksson et al. 2014; Lebzelter et al. 2014; Uttenthaler et al. 2015). In the central routines, the abundances of many important ionic and molecular species are evaluated assuming chemical equilibrium. Subsequently, the resulting partial pressures can be used to compute the continuous and line opacity at each selected frequency point (in LTE). At the moment, up to more than 175 million transitions are included in a calculation covering the complete COMARCS wavelength range. This number, which is dominated by molecular species with more than two atoms (e.g. H_2O, HCN, CO_2) or electronic transitions (e.g. TiO, CN), depends on the chosen line lists. In addition, COMA is also able to produce opacities for a considerable amount of dust types, if information concerning the degree of condensation is provided (e.g. Nowotny et al. 2011, 2015; Bladh et al. 2015). It should be noted that equilibrium abundances of solid particles are not computed, since such a situation never appears in astrophysical environments.

More information concerning the COMA code can be found in Aringer et al. (2009). In comparison to that work, we have added some new opacity sources mainly important for the structures and spectra of dwarf stars. Line lists for the hydrides MgH (Skory et al. 2003; Weck et al. 2003b), TiH (Burrows et al. 2005) and CaH (Weck, Stancil & Kirby 2003a) are now taken into account. Their features appear primarily in the visual range. For CaH and MgH, the data for the chemical equilibrium constants come from Sauval & Tatum (1984) with a revised dissociation energy of 1.285 eV for MgH (Shayesteh et al. 2007). The corresponding values for TiH were taken from Burrows et al. (2005). At this point, it should also be noted that we have changed the dissociation energy of CrH from 2.86 to 2.17 eV (Bauschlicher et al. 2001) resulting in significantly lower abundances (up to two orders of magnitude) and weaker bands of the molecule compared to Aringer et al. (2009).

Other species which have been added to the line opacity calculations are CS (Chandra et al. 1995) and CH_4. In the case of methane, COMA can currently only process the HITRAN 2008 data (Rothman et al. 2009) with a quite limited number of transitions. This is no problem for the results presented here, since the hydrostatic model atmospheres do not extend into the cool temperature ranges where CH_4 becomes important. At the moment, the following molecules are included in COMA and the line opacities used for this work: CO, CH, C_2, CS, CN, H_2O, C_2H_2, HCN, C_3, SiO, OH, TiO, VO, YO, ZrO, CO_2, SO_2, CH_4, HF, HCl, FeH, CrH, MgH, TiH and CaH.

Line lists from the HITRAN data base may be selected in COMA as an option for CO, H_2O, CO_2, OH, HF and C_2H_2, while they represent the only available source for SO_2, HCl and CH_4. In the case of OH, they are the preferred choice. In comparison to the computations described in Aringer et al. (2009), where only the 2004 version of HITRAN (Rothman et al. 2005) could be used, it is now also possible to take the data from HITRAN 2008 (Rothman et al. 2009). For the work presented here, we extracted the transitions of SO_2, HCl and CH_4 from HITRAN 2008, while we kept HITRAN 2004 for OH (better agreement with observed mid-IR spectra). In addition, COMA can process the HITEMP 2010 data for H_2O, CO_2, OH and CO (Rothman et al. 2010), which may

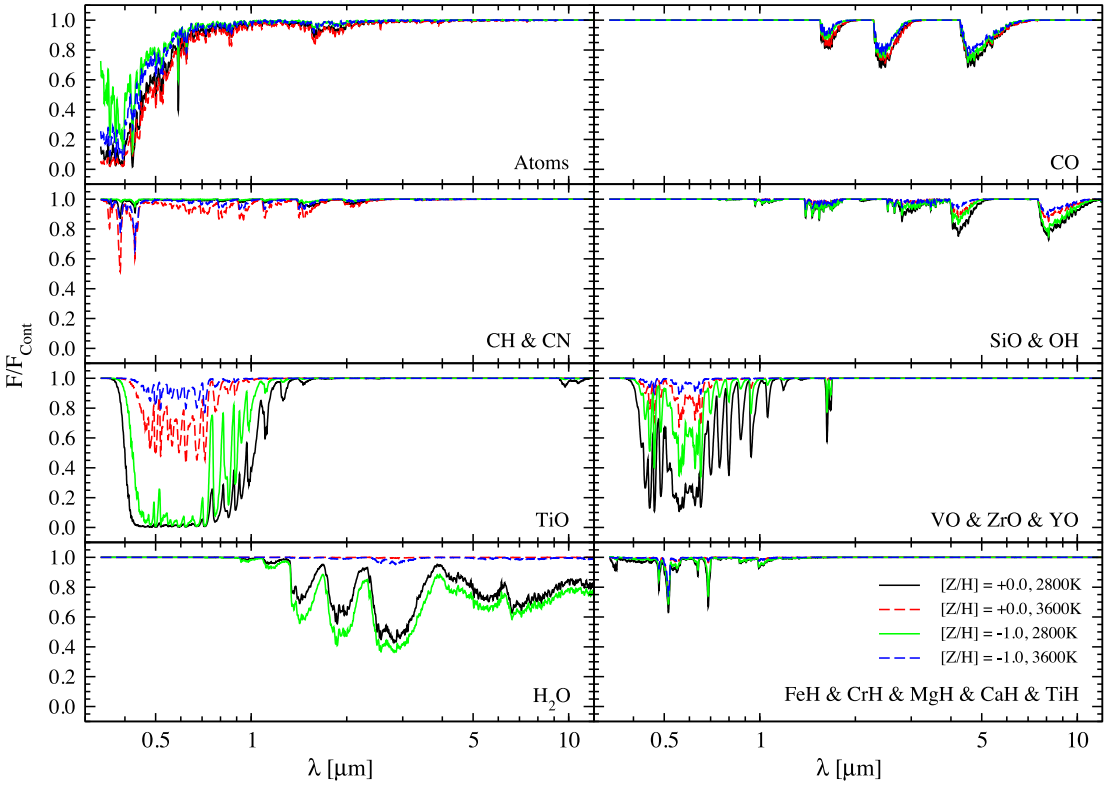

Figure 1. Continuum normalized spectra for important molecular species and atomic lines based on COMARCS models with $\log(g\,[\mathrm{cm\,s^{-2}}]) = 0.0$, $M/\mathrm{M}_{\odot} = 1.0$ and scaled solar abundances. Two different metallicities ($Z/\mathrm{Z}_{\odot} = 1.0 \rightarrow [\mathrm{Z/H}] = 0.0$, $Z/\mathrm{Z}_{\odot} = 0.1 \rightarrow [\mathrm{Z/H}] = -1.0$) and temperatures ($T_{\mathrm{eff}} = 2800$ K, solid lines, $T_{\mathrm{eff}} = 3600$ K, dashed lines) are shown.

improve the results for the first three of the molecules. However, since that option was not available when the work on the COMARCS grid was started, the HITEMP 2010 lists are not considered here. This is not a big problem, because for H_2O and OH the changes of the overall absorption and medium- or low-resolution spectra are small, if one compares to calculations with the current standard data [HITRAN for OH and BT2 from Barber et al. (2006) for water]. The update of HITEMP to the 2010 version produces some differences in the CO_2 bands around 4.4 μm. But even in the coolest COMARCS models, the features of carbon dioxide remain always very weak.

It should be mentioned that the changes discussed in the previous paragraphs do not have a significant effect on the overall opacity and atmospheric structure in the models. As in Aringer et al. (2009) Doppler profiles including the thermal and the microturbulent contribution were assumed for the molecules, while the atomic transitions are broadened with Voigt functions, if damping constants are available. In Fig. 1, we show absorption spectra of different species important for K and M stars, which are calculated from COMARCS atmospheres with $\log(g\,[\mathrm{cm\,s^{-2}}]) = 0.0$, $M/\mathrm{M}_{\odot} = 1.0$ and scaled solar abundances. Four models having solar ($Z/\mathrm{Z}_{\odot} = 1.0$) or 10 times lower ($Z/\mathrm{Z}_{\odot} = 0.1$) metallicity and $T_{\mathrm{eff}} = 2800$ or 3600 K are included. The spectra were normalized using a computation without any line opacities and have a resolution of $R = 200$. Species showing similar behaviour are combined in groups: atoms, CO, CH & CN, SiO & OH, TiO, VO & ZrO & YO, H_2O, FeH & CrH & MgH & CaH & TiH.

As one can see in Fig. 1, TiO and atoms dominate the opacities below 1 μm. The corresponding absorption increases with higher metallicity and lower temperature. Especially in cooler objects the stellar radiation is almost completely blocked in broad regions of the spectrum, which has a severe impact on the atmospheric structure. The strong heating effect caused by TiO is discussed in Aringer et al. (1997). At low temperatures, water becomes an important absorber in the whole infrared range. For solar abundances, this happens in giants cooler than 3200 K, while in dwarfs intense H_2O bands appear already at around 4200 K, since higher pressures favour the formation of polyatomic molecules. An interesting trend visible in Fig. 1 is that the features of H_2O get stronger with decreasing metallicity. This behaviour can mainly be explained by the reduced heating of the atmospheres due to TiO. In order to observe such an effect, stars with identical parameters (T_{eff}, $\log(g)$) need to be compared. However, this is not so easy, if one studies different stellar populations.

In Fig. 1, it is also obvious that at cooler temperatures there exists no point in the spectra, which is not affected by intense molecular or atomic absorption. Due to the impact of line opacities on the atmospheric structures and measurable pseudo-continua, the relation between chemical abundances and the apparent depth of spectral features may become quite complicated.

There are still some uncertainties concerning the opacity data, especially for species with a large number of transitions and at higher spectral resolutions. This can already be seen in Fig. 17 where we compare the results from different hydrostatic model approaches. The effect of changing the selected line list for TiO and H_2O in COMA is shown in Figs 2 and 3. Nevertheless, in the case of the K and M giants studied here, we do not expect that any uncertainties of the used data or possible missing opacities will have a significant influence on the overall absorption and atmospheric structures.

In Fig. 2, we compare synthetic spectra for a COMARCS model with $T_{\mathrm{eff}} = 2800$ K, $\log(g\,[\mathrm{cm\,s^{-2}}]) = 0.0$, one solar mass and solar

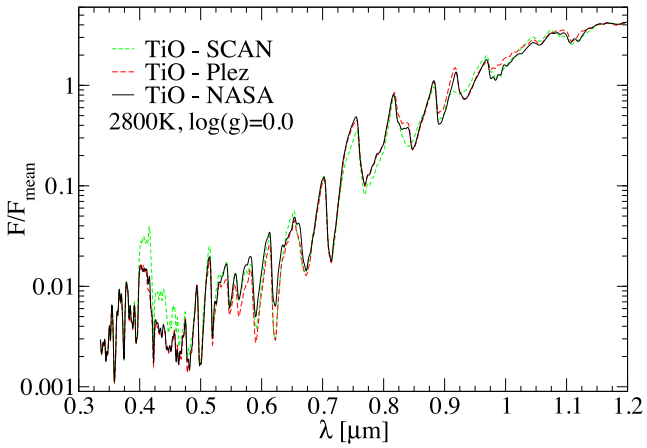

Figure 2. Spectra calculated with different TiO data based on a COMARCS model with $T_{\rm eff} = 2800$ K, $\log(g\,[{\rm cm\,s^{-2}}]) = 0.0$, one solar mass and solar metallicity. The NASA-AMES (black, used in this work as standard), Plez (red) and SCAN (green) line lists are compared. The intensities νL_ν are normalized to their mean value.

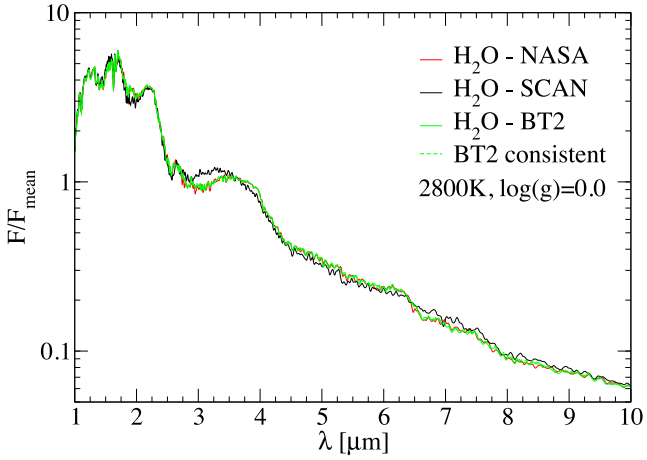

Figure 3. Spectra calculated with different H_2O data based on a COMARCS model with $T_{\rm eff} = 2800$ K, $\log(g\,[{\rm cm\,s^{-2}}]) = 0.0$, one solar mass and solar metallicity. The SCAN (black, used in this work as standard), BT2 (green, used in this work as standard) and NASA-AMES (red) line lists are compared. The intensities νL_ν are normalized to their mean value. We also show the result obtained with a consistent usage of the BT2 data for the computation of the atmospheric structure and the spectrum (green dashed), which is very similar to the one where BT2 was only taken for the a posteriori radiative transfer (green solid).

metallicity, which were calculated using different TiO data. The computations presented here are normally done with the NASA-AMES list (Schwenke 1998). In addition, we have included results obtained with the Plez (Plez 1998) and the SCAN list (Jørgensen 1994, 1997). The spectra, which do also contain the features of the other species, cover the wavelength range up to 1.2 μm at a resolution of $R = 200$. It should be noted that the same COMARCS model calculated with the NASA-AMES data was used in all three cases. This inconsistency is no problem, since the studied lists produce quite similar overall opacities and atmospheric structures. There are only some differences on smaller scales.

A similar comparison is done in Fig. 3 where we investigate the effect of using different H_2O data. The stellar parameters of the corresponding COMARCS model are the same as in Fig. 2. We present results obtained with the BT2 (Barber et al. 2006), SCAN (Jørgensen et al. 2001) and NASA-AMES (Partridge & Schwenke 1997) list. HITEMP 2010 (Rothman et al. 2010), which may be regarded as the most recent and complete collection of water lines, is not included in the plot. However, at the selected low resolution of $R = 200$, the differences between BT2 and HITEMP 2010 are rather small. It should be noted that HITEMP is partly based on the work of Barber et al. (2006). The atmospheres in the COMARCS grid are computed using the SCAN data, which represent therefore the prime choice for the calculation of the synthetic spectra. For all oxygen-rich models with temperatures cool enough that water absorption may become important, the a posteriori radiative transfer has also been done involving the BT2 list. The limit was in most of the cases set to $T_{\rm eff} = 4000$ K, but may become higher than 5000 K for dwarfs. In the plots of this paper, we show usually the results obtained with the BT2 data if available. Like for TiO, the inconsistent treatment of opacities in the calculation of COMARCS atmospheres and synthetic spectra will not cause problems, since the different lists give quite similar structures. It should be noted that this is true for hydrostatic models and the range of parameters covered by the COMARCS grid. If a significant part of the computed atmosphere extends to gas temperatures below 1000 K, SCAN and BT2 produce deviating results. The reason for this is a systematic difference in the overall absorption above 6 μm as one can see in Fig. 3. A discussion of the behaviour of SCAN and NASA-AMES in the mid-infrared and a comparison to *ISO*-SWS observations are presented in Aringer, Kerschbaum & Jørgensen (2002).

In Fig. 3, we compare two different spectra obtained with the BT2 line list. The first one is based on a standard COMARCS atmosphere, which has been calculated with the SCAN data. The second energy distribution results from a consistent usage of the BT2 opacities for the determination of the model structure and the a posteriori radiative transfer. It is obvious that the differences between the two spectra remain in all regions very small. This conclusion is also valid, if one plots the absolute intensities without normalization. The relative deviations of the frequency-integrated radiative fluxes in the various layers up to the surface caused by the inconsistent treatment of the water opacity in the first case do never exceed values around 2 per cent. This confirms that our approach concerning the BT2 spectra is not too problematic.

In addition to the new and updated line lists, we have also revised the continuous opacities by including the collision-induced absorption (CIA) of H_2–H_2 (Borysow, Jørgensen & Fu 2001; Borysow 2002), H_2–H (Gustafsson & Frommhold 2003), H_2–He (Jørgensen et al. 2000) and H–He (Gustafsson & Frommhold 2001). This is especially important for the very cool and dense dwarf atmospheres at low metallicity, while it has no effect on the structures and spectra of the giants studied here.

2.2 Model parameters

The COMARCS grid, which was mainly designed to transfer the results of stellar evolution calculations into observable properties of the various objects (e.g. Aringer et al. 2009), aims at cool stars. The typical range of effective temperatures covered by the models is between 2500 and 5000 K with values of $\log(g\,[{\rm cm\,s^{-2}}])$ extending from 5.0 to −1.0. Some hotter ($T_{\rm eff}$ up to 7170 K) and more compact ($\log(g\,[{\rm cm\,s^{-2}}])$ up to 5.32) computations are also included. An overview of the COMARCS grid can be found in Appendix A in Table A1, where we list the opacity sets available at the moment. They correspond to an input file produced by COMA and are characterized by a certain selection of elemental abundances, microturbulent velocity (ξ) and source data for the absorption. Each of them may

contain models with different effective temperature, surface gravity or mass. The range in $T_{\rm eff}$ and log (g) covered by the various sets is also listed in the table. Since the COMARCS grid is constantly growing, the information given in the Appendix A represents only a snapshot at the time when this paper was produced. An updated and complete catalogue of the available models may be obtained from http://starkey.astro.unipd.it/atm.

The central part of the COMARCS data base are several subgrids of different metallicities where the relative abundances of all elements heavier than He (Z) have been scaled in the same way. The values with reference to the Sun log ($Z/Z_{\odot}$) or [Z/H] range from -2 to $+1$ separated by steps of 0.5. The corresponding solar chemical composition is based in essence on Caffau, Ludwig & Steffen (2009a) and Caffau et al. (2009b) resulting in a C/O ratio close to 0.55. In this work, $Z/Z_{\odot}$ and [Z/H] represent the relative abundance of the bulk of metals. A variation of the amount of one or more elements like carbon or nitrogen will not change these numbers. Since the current COMARCS data base does not include opacity sets with a special scaling for iron, [Z/H] is always equal to [Fe/H]. The subgrids of different metallicities cover effective temperatures between 2600 and 5000 K with steps of 100 K or smaller, while the values of log(g [cm s^{-2}]) range from 5.0 to -1.0 with a maximum increment of 0.5. Models with log(g [cm s^{-2}]) < 0.0 were usually only computed for stars cooler than about 3500 K. The standard microturbulent velocity of the calculations was set to $\xi = 2.5$ km s^{-1}, which is in agreement with our previous work (Aringer et al. 2009, 1997) and high-resolution observations of M giants (e.g. Smith & Lambert 1985, 1990). For other groups of objects covered by the COMARCS grid, different typical ξ values will be appropriate. An example is dwarfs or RSG, which are not discussed in this paper. However, the influence of the microturbulence on the atmospheric structure and low-resolution spectra remains for most of the cooler models quite limited, if the deviations do not become too large. This is due to the huge number of weak overlapping lines that dominate the opacity. For solar metallicity, the COMARCS data base includes also calculations with $\xi = 1.5$ and 5.0 km s^{-1}. In general, the model atmospheres in the central subgrids were computed assuming the mass of the Sun. Especially for the more extended objects with log(g [cm s^{-2}]) ≤ 0.0, where sphericity effects may become important, different selections of this parameter have been considered.

Concerning the evaluation of the convective fluxes, we follow the approach described and applied by Gustafsson et al. (1975, 2008) for their MARCS models as we use the mixing length formalism from Henyey, Vardya & Bodenheimer (1965) with the same parameters ($\alpha = 1.5$, $\nu = 8.0$, $y = 0.076$). For the calculation of the turbulent pressure, we have adopted $\beta = 1.0$. The velocity of the convective elements from the equations was taken. According to Gustafsson et al. (2008), this may result in values being too high. However, the influence of the chosen turbulent pressure on our synthetic spectra and photometry is limited, since only the innermost layers are affected.

In Fig. 4, we show the subgrid of $T_{\rm eff}$ and log (g) values for the solar chemical composition. Models of different masses and microturbulent velocities are included without any further distinction. Up to 3800 K, the calculations have been extended to log(g [cm s^{-2}]) < 0.0. The high density of grid points in that region and constraints of the lower limit for the surface gravity around 3000 K are partially caused by convergence problems (Aringer et al. 2009). In the domain of the compact objects, there is a sequence of COMARCS atmospheres with effective temperatures from 5000 to 3000 K, which crosses the log(g [cm s^{-2}]) = 5.0 line. This corresponds to the zero-age main sequence (ZAMS) of dwarfs having solar chemical composition as derived from the PARSEC code (Bressan et al. 2012) for stellar evolution.

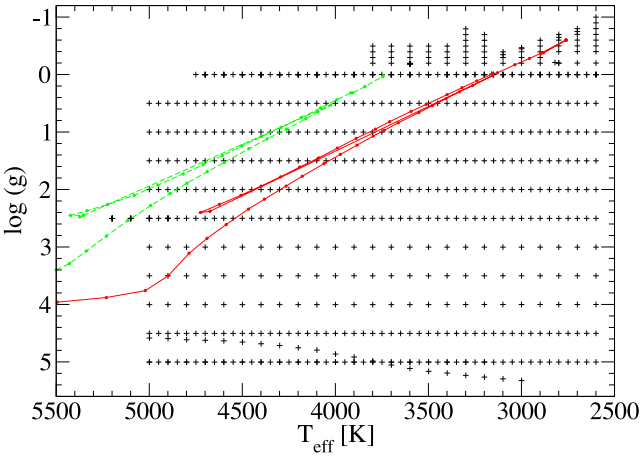

Figure 4. Values of effective temperature and log(g [cm s^{-2}]) covered by the current COMARCS grid in the case of solar abundances (crosses). Models of different masses are not distinguished. In addition, evolutionary tracks for stars with one solar mass and $Z/Z_{\odot} = 1.0$ (red solid line) as well as $Z/Z_{\odot} = 0.1$ (green dashed line) are displayed.

Fig. 4 contains also two sequences of models connected by lines, which have been placed along evolutionary tracks for stars with the mass of the Sun. The corresponding values of $T_{\rm eff}$ and log (g) were computed using PARSEC and for the latest stages the COLIBRI code (Marigo et al. 2013). They cover the whole period between the ZAMS and the final phase of the AGB. The sequences, which extend to much higher temperatures than the rest of the shown COMARCS subgrid (5940 and 7170 K), differ by their chemical composition. The first one is compatible with the other models in the figure, since it has also solar abundances. The second track, which is considerably hotter, was calculated assuming [Z/H] $= -1$. Because of intense stellar winds at the late stages of the AGB evolution that are included in the COLIBRI computations, the mass of the last few objects in the sequences is reduced (0.74 and 0.79 $M_{\odot}$ at the final point). We have taken this effect into account when producing the COMARCS models.

As one can see in Table A1, the COMARCS data base contains also opacity sets where the abundances of individual elements have been changed separately. The most important example is the amount of carbon, which is specified here by the C/O ratio. This varies during the late stages of stellar evolution due to several nucleosynthesis and dredge-up processes (e.g. Busso, Gallino & Wasserburg 1999; Cristallo et al. 2011). The data include a number of subgrids and sequences computed with C/O values different from the one associated with the solar composition (0.55), which cover the interval between 0.25 and 10.0. Models were usually produced for those combinations of effective temperature and surface gravity where the corresponding intrinsic modifications of the abundances are expected. As an example, there was no need to take dwarfs into account. This results in subgrids much smaller than the ones with a metallicity scaled solar composition. The opacity sets for carbon stars (C/O > 1) are listed in the end of Table A1. The models therein will replace the data base of Aringer et al. (2009).

The COMARCS data allow one to also investigate the effect of an increased nitrogen abundance. Models with [N/Z] $= +1$ exist for two different metallicities: [Z/H] $= 0$ and -1. At the moment, sequences with log(g [cm s^{-2}]) $= 0.0$ and $+2.0$ covering temperatures between 2600 and 5000 K as well as COMARCS atmospheres placed

along an evolutionary track of a star with one solar mass (see Fig. 4 and text above) are available. The effects of enhancing nitrogen and changing C/O will be discussed in the next sections.

2.3 Synthetic spectra and photometry

For the complete grid of hydrostatic COMARCS atmospheres, we computed synthetic opacity sampling spectra covering the range between 400 and 29 814.7 cm^{-1} (0.3354–25.0 μm) with a resolution of $R = 10\,000$. Following the approach described in Aringer et al. (2009) or Nowotny et al. (2011) for carbon stars, we used the COMA code in combination with an attached spherical radiative transfer program (Windsteig et al. 1997). Except for the denser distribution of frequency points, the treatment of the continuous and line absorption was in general consistent with the input data for the production of the models. As is discussed in Section 2.1, that is not valid for the spectra, which have been calculated involving the BT2 list for water. However, this does not create a severe problem, since the different applied H_2O data result in similar hydrostatic structures.

Because of the statistical nature of the opacity sampling approach, only the average over a larger number of frequency points (about 20 to 100) ensures a realistic representation of the observed stellar spectra (Nowotny et al. 2011). Thus, we decreased the resolution of the output of the radiative transfer code to $R = 200$ by convolving it with a Gaussian function. We did not include any additional line broadening induced for example by a macroturbulent velocity. The wavelength grid has been done with a spacing corresponding to $R = 2000$ resulting in a smooth appearance of the final spectra. The same procedure was already used by Aringer et al. (2009) to obtain their low-resolution data. Examples for the output can be found in Figs 1, 2, 3 and 17. The spectra are electronically available as described in Section 3.2.

We also produced synthetic bolometric corrections for a large set of filters following the same formalism as described in Girardi et al. (2002, equations 7 and 8). First, we convolved the transmission curve with the calculated opacity sampling spectra. This was done with an integration of the energy or the number of detected photons depending on if amplifiers or counting devices were used for the definition of the investigated photometric system. Subsequently, the obtained magnitudes were scaled with respect to a reference intensity in order to consider the zero-points. This quantity was determined from a convolution with the filter curve applied to a constant flux per unit wavelength (frequency) in the case of STmag (ABmag) systems or to a Vega (α Lyr) spectrum for Vegamag data. We took the energy distribution of the standard star from the work of Bohlin (2007). The corresponding values are expected to be accurate to within about 2 per cent in the optical and near-infrared range. The latest table of synthetic bolometric corrections is electronically available as described in Section 3.3.

3 RESULTS

In this section, we want to present some results obtained using the COMARCS grid with special emphasis on the effects of C/O ratio, nitrogen abundance and stellar mass. The impact of these quantities on the atmospheric structures, spectra and colours will be discussed. It can be regarded as a correction that has to be applied to the properties of a star predicted from the main parameters, which are temperature, surface gravity and overall metallicity (see Section 4.3). We investigate where the mentioned effects become important. As was already stated, the values of C/O and [N/*Z*] change during the late stages of stellar evolution. If the C/O ratio exceeds 1, a severe modification of the atmospheric structure and spectral appearance happens, since the object turns into a carbon star. However, this case will not be considered here, because we focus on K and M giants. The evolutionary tracks for one solar mass shown in Fig. 4 that are used for some plots of this paper do also not reach C/O $\geq$ 1.0. An enhancement of s-process elements like Y or Zr, which is often connected to an increased C/O value, is as well not discussed, since we do not cover S stars in our study. The properties of the latter group of objects are investigated by van Eck et al. (2011).

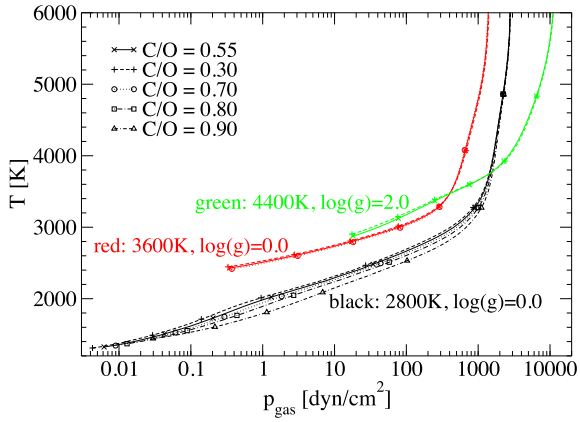

Figure 5. The effect of the C/O ratio on the atmospheric temperature versus gas pressure structure is shown for different COMARCS models with solar mass and metallicity. Three examples are included: $T_{\rm eff} = 2800$ K, $\log(g\,[{\rm cm\,s^{-2}}]) = 0.0$ (black) with C/O = 0.30, 0.55, 0.70, 0.80, 0.90, $T_{\rm eff} = 3600$ K, $\log(g\,[{\rm cm\,s^{-2}}]) = 0.0$ (red) with C/O = 0.30, 0.55, 0.70 and $T_{\rm eff} = 4400$ K, $\log(g\,[{\rm cm\,s^{-2}}]) = 2.0$ (green) with C/O = 0.30, 0.55. C/O = 0.55 corresponds to the solar value. The plot symbols placed along the different curves mark steps of $\Delta\log(\tau_{\rm Ross}) = 1$ starting with −5 at the outer edge.

3.1 Atmospheric structure

In Fig. 5, we present the atmospheric temperature pressure structure of various hydrostatic models taken from the COMARCS grid, which have the mass and overall metallicity of the Sun. For three different combinations of $T_{\rm eff}$ and log (g), the effect of changing the C/O ratio is shown. Values between 0.3 and 0.9 are covered including 0.55 for the solar composition. Models with a high C/O exceeding 0.7 are only available for the coolest set with $T_{\rm eff} = 2800$ K and $\log(g\,[{\rm cm\,s^{-2}}]) = 0.0$. Such a large relative enhancement of carbon can appear during and after the AGB phase as a consequence of the third dredge-up (Busso et al. 1999; Cristallo et al. 2011). The additional combinations are $T_{\rm eff} = 3600$ K with $\log(g\,[{\rm cm\,s^{-2}}]) = 0.0$ and $T_{\rm eff} = 4400$ K with $\log(g\,[{\rm cm\,s^{-2}}]) = 2.0$. The figure shows that there is a clear trend of colder structures with increasing C/O ratio, but significant changes happen solely above 0.7. The latter may be partly explained by the fact that the amount of oxygen atoms not bound in CO gets more crucial for the formation of other species like TiO or H_2O, if it becomes very low. However, one should always keep in mind that the relations can be quite complicated, if molecules important for the overall opacity are involved. For example, the abundance of TiO, which causes a strong heating of the atmospheres, decreases in the inner regions of the models having $T_{\rm eff} = 2800$ K and $\log(g\,[{\rm cm\,s^{-2}}]) = 0.0$ at higher C/O values, while it grows in the outer areas below $T_{\rm gas} = 2400$ K.

In Fig. 6, we demonstrate how increasing the nitrogen abundance by a factor of 10 affects the atmospheric temperature pressure

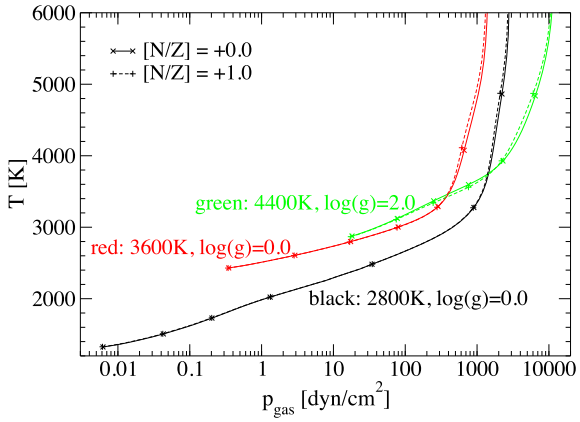

Figure 6. The effect of the nitrogen abundance on the atmospheric temperature versus gas pressure structure is shown for different COMARCS models with solar mass and metallicity. Three examples are included: $T_{\rm eff} = 2800$ K, $\log(g\,[{\rm cm\,s^{-2}}]) = 0.0$ (black), $T_{\rm eff} = 3600$ K, $\log(g\,[{\rm cm\,s^{-2}}]) = 0.0$ (red) and $T_{\rm eff} = 4400$ K, $\log(g\,[{\rm cm\,s^{-2}}]) = 2.0$ (green). [N/Z] = 0.0 (solid) corresponds to the solar value of $\log(\varepsilon_{\rm N}/\varepsilon_{\rm H}) + 12 = 7.90$ and [N/Z] = +1.0 (dashed) to N enhanced by a factor of 10. The plot symbols placed along the different curves mark steps of $\Delta\log(\tau_{\rm Ross}) = 1$ starting with −5 at the outer edge.

structure. This enhancement can be regarded as typical for the late stages of stellar evolution, since the maximum values predicted by codes like COLIBRI (Marigo et al. 2013) range between about 2 and 100 depending on mass and composition. We show three sets of models with the same parameters as the ones used in Fig. 5 for the C/O ratio. It is obvious that the impact of changing [N/Z] remains in general small. It disappears almost completely for the coolest objects, where the CN bands become weaker and their importance is additionally reduced by the intense absorption of other species like TiO or water.

3.2 Spectra

The complete grid of our $R = 10\,000$ opacity sampling and convolved low-resolution $R = 200$ spectra computed from the COMARCS models can be found at http://starkey.astro.unipd.it/atm. The corresponding tables consist of three columns: wavelength [Å], continuum normalized flux and specific luminosity times frequency (νL_ν [erg s^{-1}]). The second quantity is obtained from dividing the result of a full radiative transfer calculation by one where the atomic and molecular line absorption is totally neglected. This allows one to evaluate the apparent intensity of the various spectral features. However, such continuum normalized data should be interpreted with care, since the optical depth scale changes when opacities are removed. An example can be seen in Fig. 1, where we investigate the contribution of different species to the total absorption. In this case, a calculation including only the corresponding transitions was divided by one without any lines. The resolution is again $R = 200$. We want to emphasize that the $R = 10\,000$ opacity sampling spectra must not be directly compared to observations as was explained in Section 2.3. The parameters used to characterize the different entries in our data base can be found in Section 3.3, where we describe the tables with the synthetic photometry.

In the following sections, we study the changes of the $R = 200$ spectra caused by different C/O ratios, nitrogen abundances and masses. This is done by normalizing them with a calculation where the investigated parameters have solar values.

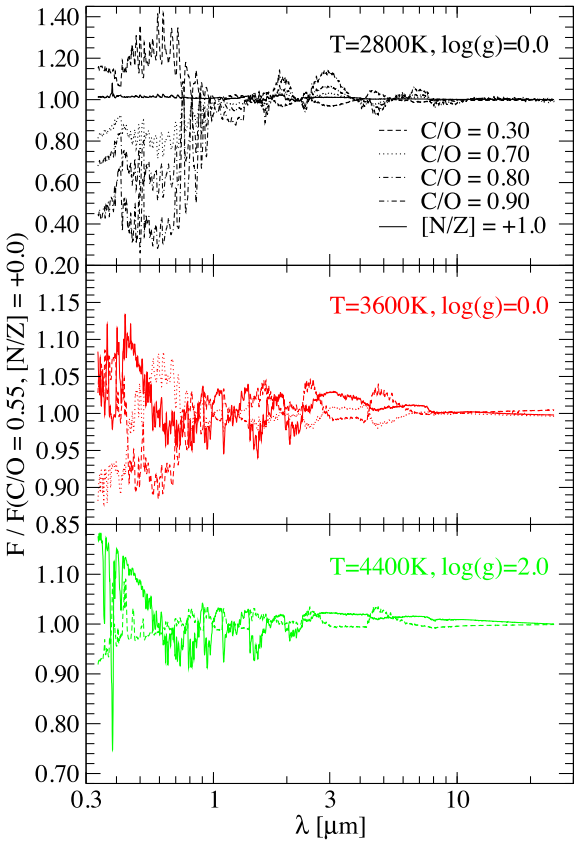

Figure 7. Relative spectral changes due to different C/O ratios and an increased nitrogen abundance for COMARCS models with solar mass and metallicity. The spectra are normalized to a calculation with solar composition (C/O = 0.55, $\log(\varepsilon_{\rm N}/\varepsilon_{\rm H}) + 12 = 7.90$). Three examples are included: $T_{\rm eff} = 2800$ K, $\log(g\,[{\rm cm\,s^{-2}}]) = 0.0$ (upper panel) with C/O = 0.30, 0.70, 0.80, 0.90, [N/Z] = +1.0, $T_{\rm eff} = 3600$ K, $\log(g\,[{\rm cm\,s^{-2}}]) = 0.0$ (middle panel) with C/O = 0.30, 0.70, [N/Z] = +1.0 and $T_{\rm eff} = 4400$ K, $\log(g\,[{\rm cm\,s^{-2}}]) = 2.0$ (lower panel) with C/O = 0.30, [N/Z] = +1.0.

3.2.1 C/O ratio and nitrogen abundance

In Fig. 7, one can see what happens if the nitrogen abundance increases by a factor of 10 and the C/O value changes to 0.3, 0.7, 0.8 or 0.9. In order to emphasize the effects, the spectra are normalized using a calculation with solar chemical composition implying C/O = 0.55 and [N/Z] = 0. The figure has three panels with different combinations of temperature and surface gravity. The corresponding sets of COMARCS models are equal to the ones described in Section 3.1 and appearing in Figs 5 and 6. Only the computations with solar abundances are missing, since they have been used for the normalization. Thus, they would get a constant value of one in the plot.

For the coolest of the shown sets with $T_{\rm eff} = 2800$ K and $\log(g\,[{\rm cm\,s^{-2}}]) = 0.0$, there exists a clear trend. The absorption at short wavelengths dominated by TiO and atoms increases with higher C/O values, while the water bands above 1.8 μm become weaker. Considerable differences appear especially in the optical range. The flux in the *V* filter varies by a factor of about 3, if C/O grows from 0.3 to 0.9. But even a moderate change from solar composition to C/O = 0.3 or 0.7 causes deviations of ±20 per cent. The relation between atmospheric structure, chemical equilibrium and molecular absorption is often not simple. As has already been mentioned in Section 3.1, the abundance of TiO, which produces

a strong heating, decreases in the inner regions of the models at higher C/O ratios, while it grows in the outer areas below 2400 K.

An enhancement of nitrogen has almost no effect on the spectra of the coolest set. As one can see in Fig. 1, this is mainly due to the weakness of the CN bands appearing at lower temperatures. Also the large opacities of TiO and water in the outer regions of the cold atmospheres play a role. In K and M giants, CN is the most important molecule contributing to the absorption, which includes nitrogen. The situation becomes quite different in the warmer sets with 3600 and 4400 K, where [N/Z] has some influence. In these cases, an increased value causes deeper CN bands and weaker atomic features. In general, the variations produced by the investigated changes of the composition are smaller at the higher temperatures. Apart from a few exceptions, they never exceed ±10 per cent in the two warmer sets. However, one should not forget that at 3600 and 4400 K the C/O ratios above 0.7 are not covered.

Concerning the behaviour as a function of the C/O value, there is a clear trend in the spectra of the warmer sets. The depth of the CO bands in the near- and mid-infrared increases with a higher ratio, which can be explained by the fact that more carbon becomes available to form the molecule. This effect appears already at 2800 K, where it is less pronounced due to the contamination with the opacity of water. In the models with 3600 K, the absorption around 0.6 μm, which is dominated by TiO, gets weaker, if the C/O value grows. This is the opposite of the behaviour observed for the coolest set and an example for a more complex relation, where trends may be reversed when changing the basic stellar parameters. Thus, one should always be careful, if abundance corrections to synthetic spectra or photometry determined for a certain combination of effective temperature and surface gravity are transferred to models with different properties. At 2800 and 3600 K, the intensity of the atomic absorption below 0.5 μm increases with a higher C/O ratio. Also this trend does not appear in all places, as one can see looking at the 4400 K set in the plot.

The significance of the excess of oxygen compared to carbon (O−C) for the spectra and atmospheric structures at a changing C/O ratio is discussed in Appendix B. Especially in cooler models, this parameter will be important, since most of the C atoms form CO molecules.

3.2.2 *Mass*

In Fig. 8, we investigate the impact of the stellar mass on our COMARCS spectra. If the effective temperature and surface gravity are fixed, this parameter represents the degree of sphericity in a hydrostatic atmosphere. It causes changes, which are in general much smaller than the ones connected to the two other mentioned quantities. Thus, the corresponding deviations can also be treated as a correction applied to the result of an interpolation in the main variables, when using the COMARCS grid to determine observable properties of stars (see Section 4.3). In Fig. 8, we show spectra, which are normalized relative to a calculation with one solar mass. This helps to identify the changes caused by the investigated parameter. Two sets of models with the chemical composition of the Sun are presented, which are characterized by their effective temperature and surface gravity. The first one was taken from the stellar evolution track described in Section 2.2 and displayed in Fig. 4. With $T_{\rm eff} = 2761$ K and $\log(g\,[{\rm cm\,s^{-2}}]) = -0.6$. it is typical for a very extended late AGB star. Masses between 0.74 and 99 $M_\odot$ are covered. The smallest value corresponds to the result from the evolutionary track, if the loss of material due to stellar winds is

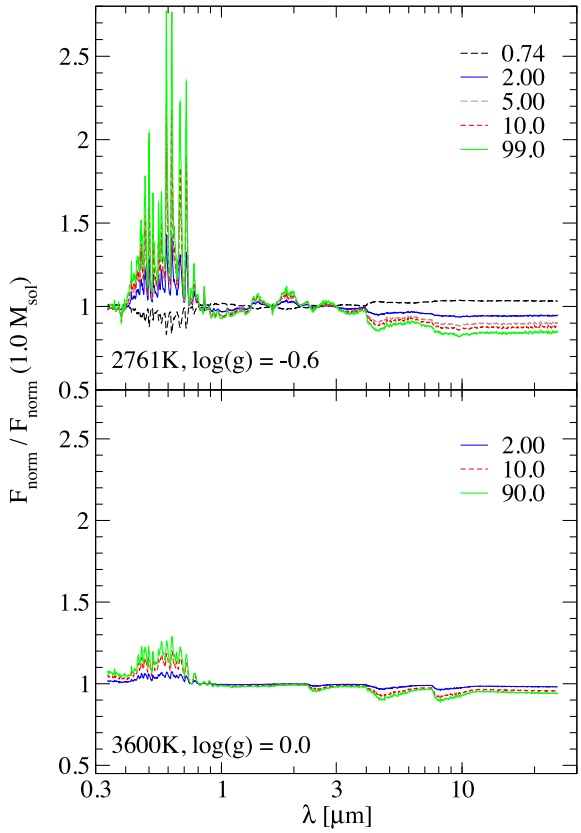

Figure 8. Relative spectral changes due to different stellar mass for COMARCS models with solar abundances. The spectra are normalized to a calculation with $M/{\rm M}_\odot = 1.0$. The effects are shown for parameters typical for a late AGB object ($T_{\rm eff} = 2761$ K, $\log(g\,[{\rm cm\,s^{-2}}]) = -0.6$, upper panel) and an RSG or RGB star ($T_{\rm eff} = 3600$ K, $\log(g\,[{\rm cm\,s^{-2}}]) = 0.0$, lower panel).

considered. It should be noted that in the used PARSEC and COLIBRI models, this effect plays only a significant role during the last stages of the AGB phase. The parameters of the second set having $T_{\rm eff} = 3600$ K and $\log(g\,[{\rm cm\,s^{-2}}]) = 0.0$ are close to the regions, where one can find RSG or RGB stars, with the latter being typically a bit more compact. In this case, masses between 2 and 90 $M_\odot$ are shown. The very high values were chosen to simulate a plane-parallel environment.

For both sets shown in Fig. 8, we observe the same trend. The intensity of the TiO bands in the optical range increases with lower mass, while the molecular absorption in the mid- and far-infrared becomes smaller. This weakening affects in the cooler models mainly the water opacity and in the warmer ones the features of CO and SiO. It can be explained by a geometric phenomenon. A lower mass causes a larger contribution of the optically thin edges of a star to the total flux, which produces more intense emission components in the lines. These may be directly observed in the profiles of different transitions especially in the infrared, if one studies high-resolution spectra of pulsating giants with a radial and temporal variation of the velocity fields (e.g. Alvarez et al. 2001; Nowotny et al. 2010). Due to an increased atmospheric extension, the effect will become very pronounced in dynamical objects with significant stellar winds. It is usually stronger at the longer wavelengths, where one might in some cases even get broad emission features (e.g. Matsuura et al. 2002; Gautschy-Loidl et al. 2004). In our hydrostatic COMARCS models with no mass-loss or velocity fields, we obtain only the mentioned weakening of the lines.

The changes of the TiO bands visible in Fig. 8 are caused by differences of the atmospheric structure. As one would expect, all effects of mass are much larger for the more extended cooler set, since they depend a lot on the surface gravity. If $\log(g\,[\mathrm{cm\,s^{-2}}])$ grows above zero, they become quickly very weak. Thus, the sphericity needs only to be taken into account during the last (and maybe first) stages of stellar evolution. However, such stars are often far away from hydrostatic equilibrium.

3.3 Synthetic photometry

The synthetic photometry computed for the complete grid of our hydrostatic COMARCS models can be found at http://starkey.astro.unipd.it/atm. The tables contain the bolometric corrections (BC) described in Section 2.3 as a function of the stellar properties. The corresponding main parameters are $T_{\rm eff}$, $\log(g\,[\mathrm{cm\,s^{-2}}])$, $M/\mathrm{M}_{\odot}$, [Fe/H], [O/H], [C/H], ξ $[\mathrm{km\,s^{-1}}]$ and a flag for the used water absorption data (SCAN or BT2, see Section 2.1). [Fe/H] which represents [*Z*/H] as well as [O/H] and [C/H] which determine the C/O ratio are listed with the absolute abundances scaled relative to hydrogen $\log(\varepsilon_{\rm Fe,O,C}/\varepsilon_{\rm H}) + 12$. Other quantities like [N/H], [Y/H] or [Zr/H] were included, if they deviate from the standard values. The opacity sets available at the moment in the COMARCS grid can be found in Table A1.

The complete set of tables covers the bolometric corrections for more than 40 photometric systems, which are separated into different files containing the values of all included filters and COMARCS models. This wealth of information may be exploited by the users of the data base. In the current work, we will only discuss the visual and near-infrared magnitudes that were determined according to the definition from Bessell (1990) and Bessell & Brett (1988). The *V*, *I*, *J*, *H* and *K* values and corresponding colours, which appear in the following sections and figures, are based on this photometric system (Bessell). The mentioned filters have been used for a large number of observations.

The observed colours of many cool and variable stars are severely affected by reddening due to circumstellar dust (Nowotny et al. 2011). Since hydrostatic model atmospheres do not take this process into account, the corresponding corrections have to be applied a posteriori to the results (Marigo et al. 2008). However, in such cases, it is preferable to use dynamical calculations describing pulsation and mass-loss.

In Figs 9–12, the colours $(V-K)$, $(V-I)$, $(J-K)$ and $(J-H)$ are presented as a function of the effective temperature for COMARCS atmospheres with solar metallicity. We compare results obtained with a C/O ratio of 0.3, 0.7 and 0.9, $[N/Z] = +1.0$, 90 $\mathrm{M}_{\odot}$ as well as $\log(g\,[\mathrm{cm\,s^{-2}}]) = 2.0$ to a standard model having $\log(g\,[\mathrm{cm\,s^{-2}}]) = 0.0$, 1.0 $\mathrm{M}_{\odot}$ and the chemical abundances of the Sun. In addition, we show the consequences of using the SCAN water data instead of BT2 for stars cooler than 4000 K (see Section 2.1). Calculations with $\log(g\,[\mathrm{cm\,s^{-2}}]) = 2.0$ are only included in the plots for $(J-K)$ and $(J-H)$, since these colours are more affected by the surface gravity.

3.3.1 *C/O ratio*

As one can see in Figs 9 and 10, $(V-K)$ and $(V-I)$ show a quite similar behaviour, if the value of C/O is changed. Below 3000–3100 K, the colours at higher ratios become significantly redder. For the coolest models and C/O = 0.9, the deviations grow up to +2 mag in $(V-K)$ and +1 mag in $(V-I)$. When the effective temperatures exceed the mentioned limit, the trend reverses. We obtain bluer

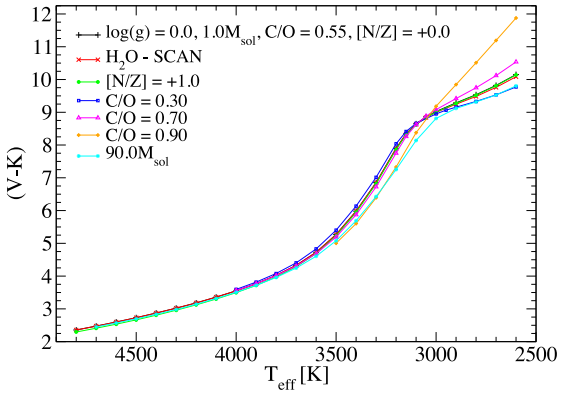

Figure 9. $(V-K)$ as a function of the effective temperature for COMARCS models with solar metallicity and $\log(g\,[\mathrm{cm\,s^{-2}}]) = 0.0$. The standard parameters are $M/\mathrm{M}_{\odot} = 1.0$, solar abundances (C/O = 0.55, [N/Z] = 0.0) and usage of the BT2 line list for water below 4000 K (black). The result of changing C/O to 0.3 (blue), 0.7 (magenta) and 0.9 (orange), of increasing nitrogen by a factor of 10 ([N/Z] = +1.0, green) or the mass to 90 $\mathrm{M}_{\odot}$ (cyan) is shown. In addition, we demonstrate the effect of taking the H_2O opacities from the SCAN data (red).

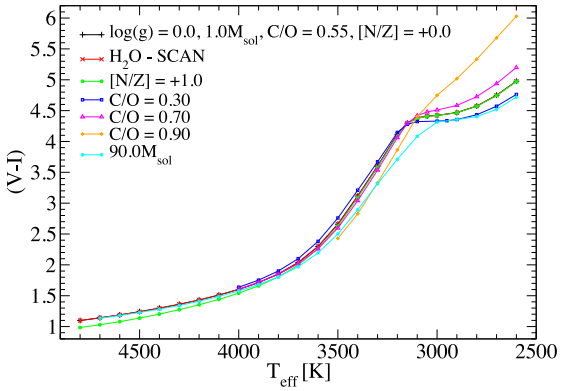

Figure 10. $(V-I)$ as a function of the effective temperature for COMARCS models with solar metallicity and $\log(g\,[\mathrm{cm\,s^{-2}}]) = 0.0$. Parameters, symbols and lines are like in Fig. 9.

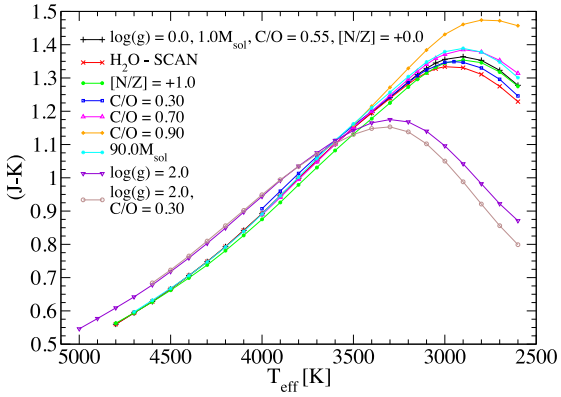

Figure 11. $(J-K)$ as a function of the effective temperature for COMARCS models with solar metallicity. The standard parameters are $\log(g\,[\mathrm{cm\,s^{-2}}]) = 0.0$, $M/\mathrm{M}_{\odot} = 1.0$, solar abundances (C/O = 0.55, [N/Z] = 0.0) and usage of the BT2 line list for water below 4000 K (black). The result of changing C/O to 0.3 (blue), 0.7 (magenta) and 0.9 (orange), of increasing nitrogen by a factor of 10 ([N/Z] = +1.0, green) or the mass to 90 $\mathrm{M}_{\odot}$ (cyan) is shown. In addition, we demonstrate the effect of taking the H_2O opacities from the SCAN data (red) and of adopting $\log(g\,[\mathrm{cm\,s^{-2}}]) = 2.0$ with C/O = 0.55 (violet) or 0.3 (brown).

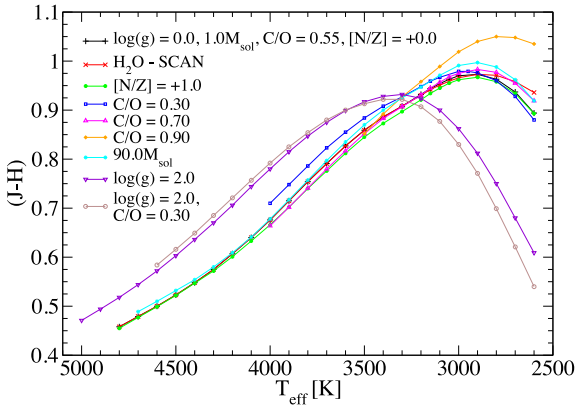

Figure 12. $(J - H)$ as a function of the effective temperature for COMARCS models with solar metallicity. Parameters, symbols and lines are like in Fig. 11.

colours for an increasing C/O ratio, although the changes always remain smaller than in the colder giants. Even at C/O = 0.9, the absolute values stay below about 0.5 mag in $(V - K)$ and 0.3 mag in $(V - I)$. The behaviour observed here is mainly caused by a variation of the TiO absorption in the V filter, which has been discussed in Section 3.2.1. In the cooler models, the intensity of these molecular bands increases with a higher C/O ratio creating redder colours, while for warmer temperatures the opposite trend may appear (see Fig. 7).

The $(J - K)$ colour shown in Fig. 11 also gets redder, if the C/O value is increased in cooler objects. This phenomenon appears at effective temperatures below about 3400 K and for both surface gravities included in the plot. At C/O = 0.9, the deviations may become quite large exceeding +0.15 mag in the coldest giants. They are mainly due to a weakening of the water bands above 1.8 μm with higher C/O ratios as is discussed in Section 3.2.1 and visible in Fig. 7, since this produces more flux in the K filter. In the models warmer than 3400 K, changes of the C/O value cause only very small variations of the $(J - K)$ colour.

The relation between $(J - H)$ and C/O is a bit more complex. Like for $(J - K)$, the colour index of the coolest models increases with the ratio. As one can see in Fig. 12, this clear trend disappears for the objects with $\log(g\,[\mathrm{cm\,s^{-2}}]) = 0.0$ and a low C/O value already at 2900 K, while it continues up to 3200 K for the compact and carbon-rich sequences. At higher effective temperatures, we even observe a reversion of the behaviour: the stars with C/O = 0.3 are predicted to be significantly redder than those with a larger ratio. This phenomenon is especially pronounced in the more extended models, where it appears above 3300 K. The increase of the colour index may exceed +0.03 mag and correspond almost to a 100 K shift of the effective temperature. The studied changes of $(J - H)$ are mostly due to variations of the CO bands and in cooler objects of the water absorption.

3.3.2 *Nitrogen abundance*

Among the four colour indices investigated here, only $(V - I)$ is significantly changed by an enhancement of nitrogen. Models warmer than 4000 K get bluer, if the abundance of that element increases. As one can see in Fig. 10, the shift for [N/Z] = +1.0 may exceed 0.1 mag, which corresponds to a difference of the effective temperature growing up to about between 100 and 200 K in this range. Looking at Fig. 7, it becomes clear that the deviations of $(V - I)$ are due to a combination of weaker atomic absorption in the V and deeper CN features in the I filter, if nitrogen is more enhanced. Below 4000 K, the changes disappear completely.

An increase of the CN band intensity with a higher nitrogen abundance may also produce small variations of the $(J - K)$ and $(J - H)$ colours. It is shown in Figs 11 and 12 that the models in the range between 3200 and 4200 K get bluer for [N/Z] = +1.0. However, these changes are not significant, since they always remain clearly below the level equivalent to a 50 K difference of the effective temperature.

3.3.3 *Mass*

In order to study the effects of sphericity, we compare in Figs 9–12 models calculated with 90 $M_\odot$ to the ones in the standard sequence having the mass of the Sun. The high value was chosen, since it produces results close to a plane-parallel solution. The corresponding colour shifts also represent in most cases an upper limit for the changes expected at a certain combination of effective temperature, surface gravity and chemical abundances. One can see in Fig. 8 that the variation of the spectra as a function of the mass is monotonous and regular. As has been mentioned in Section 3.2.2, the deviations caused by sphericity increase a lot, when the value of log (g) becomes lower. Above $\log(g\,[\mathrm{cm\,s^{-2}}]) = 0.0$, they disappear very soon.

The colour indices $(V - K)$ and $(V - I)$ presented in Figs 9 and 10 show a very similar behaviour. Below 3700 to 3800 K the models become bluer, when the mass increases. The maximum shift between 1.0 and 90 $M_\odot$, which appears around 3200 K, exceeds 0.5 mag in $(V - K)$ and 0.4 mag in $(V - I)$. As has been noted before, these deviations will grow at lower surface gravity. The bluer colours are mainly caused by the weakening of the TiO bands in the V filter, which is visible in Fig. 8.

One can see in Figs 11 and 12 that the changes of $(J - K)$ and $(J - H)$ due to sphericity effects also resemble each other. Below about 3500 to 3600 K, the colours get redder as the mass increases. In the cooler stars, this is at least partly caused by a variation of the water absorption. However, for the surface gravity used in the plots, the deviations never become very pronounced.

3.3.4 *Water opacity and general remarks*

As one would expect $(V - I)$ is not and $(V - K)$ almost not affected by the selection of the water list, since there exists no significant absorption of this molecule below 1.0 μm, while the changes in the K filter visible in Fig. 3 are small compared to the colour shifts due to a different temperature. For $(J - K)$ and $(J - H)$, we find some moderate deviations appearing in the coolest models, which can in both cases reach values of about 0.05 mag. When the SCAN data are used, $(J - K)$ becomes bluer and $(J - H)$ redder. For the giants investigated here, the changes occur only below 3000–3100 K. At this point, we want to note that because of uncertainties concerning the stellar parameters and possible deviations from hydrostatic structures with spherical symmetry as well as from LTE, which appear in cool stars, it is not easy to select the preferable line list by studying the available infrared observations.

Compared to the effects of temperature, surface gravity and metallicity, the variations due to changes of the C/O ratio, nitrogen abundance and mass are usually smaller. However, in many regions of the HRD, they are not negligible. Thus, they need to be included at least as correction factors when deriving synthetic spectra and

photometry from grids of models. An exception is C/O values close to 1 in cool stars, where large deviations of the observable properties may appear. But in those objects also the enhancement of s-process elements has to be considered, which will mainly result in much deeper ZrO bands. As we have already mentioned before, this effect is not covered in the current work. More information on models of S-type giants can be found in van Eck et al. (2011).

4 DISCUSSION

In the following text, we investigate the photometric results obtained from the COMARCS grid, which are described in Section 3.3, regarding observations and the application in connection with stellar evolution calculations. Three aspects will be discussed. First, we present a comparison to empirical colour–colour and semi-empirical colour–temperature relations from the literature. Secondly, the observed and simulated photometric properties of stars in the Galactic bulge are studied. Finally, we explore the general use of the data base in association with results from synthetic stellar evolution to describe larger samples of objects.

4.1 Comparison with observed relations

Using a large collection of observational material available in the literature, Worthey & Lee (2011) have produced a data base relating different colours with each other and with the main stellar parameters. We have applied their tables in combination with the connected interpolation routines to calculate the photometric properties of the stars situated on the evolutionary track for solar mass and abundances, which is described in Section 2.2 and shown in Fig. 4. The results can be compared to the ones obtained from our COMARCS models. Especially the colour–colour relations are interesting, since they were directly taken from the observations with a minimum of additional assumptions. One of these conditions is that the chemical abundances are known and correspond to a solar mixture scaled with the metallicity.

In Fig. 13, we show $(J - K)$ and $(V - I)$ as a function of $(V - K)$, which is in general considered to be a good indicator for the effective temperature. In addition to the results obtained from the COMARCS atmospheres and the routine from Worthey & Lee (2011), we have also included the position of the Sun according to Bessell et al. (1998). The agreement between the observed and synthetic colour–colour relations presented in the plots is in most of the cases quite satisfactory. Significant deviations appear only in $(V - I)$ for stars cooler than about 3200 K, where our models are bluer at constant $(V - K)$. However, for such cold giants, one should expect differences. Most of them show strong variations, which is a problem, if no simultaneous photometric measurements are available. Since the connected pulsations also create considerable deviations from hydrostatic structures, the predictions based on the COMARCS atmospheres and the existing abundance determinations can often not be trusted (e.g. Lebzelter et al. 2014). In addition, many of the objects are reddened by circumstellar dust, and the effects of mass and a changed C/O ratio discussed in Section 3.3 and modifying the TiO band intensity have to be taken into account.

In Fig. 14, we show the $(J - K)$ and $(I - K)$ colours as a function of the effective temperature. The predictions taken from our COMARCS models are again compared to values based on observations. The corresponding relations from Worthey & Lee (2011) have been derived using a number of sources involving various

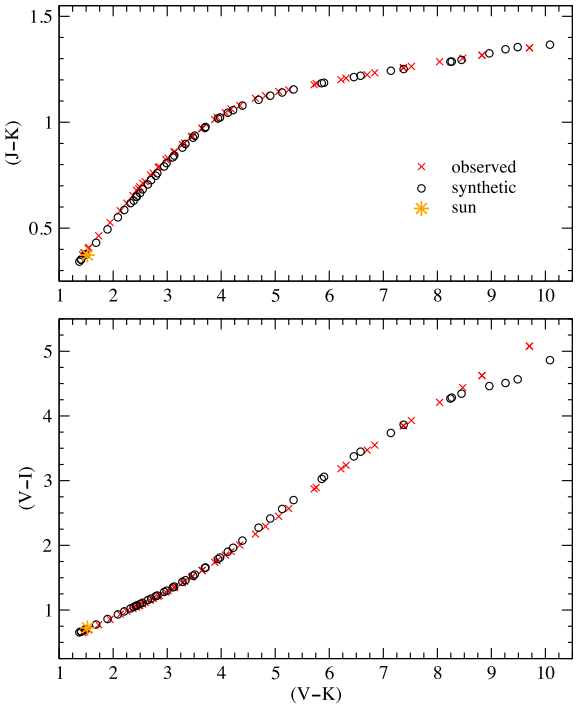

Figure 13. Two-colour diagrams $(J - K)$ and $(V - I)$ versus $(V - K)$ for stars placed along an evolutionary track with one solar mass and $Z/Z_{\odot} = 1.0$ (see Fig. 4). The results for a sequence of COMARCS models (black circles) are compared to the corresponding values taken from the fit routines by Worthey & Lee (2011), which are based on a large collection of observational material (red crosses). The colours of the Sun according to Bessell et al. (1998) are also shown (yellow stars).

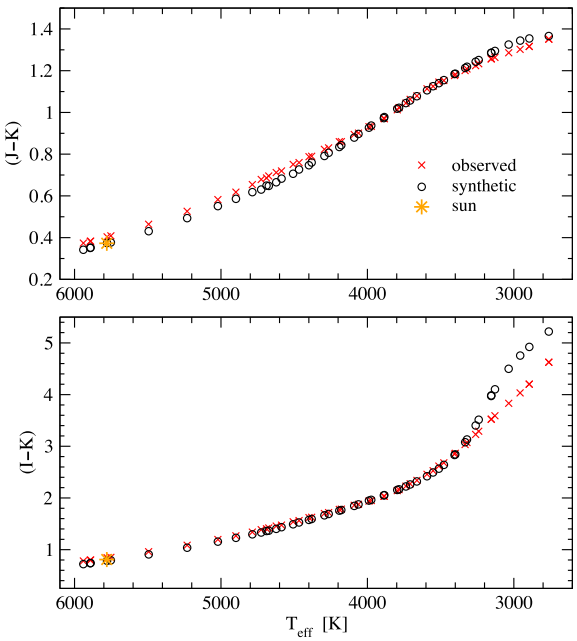

Figure 14. $(J - K)$ and $(I - K)$ as a function of the effective temperature for stars placed along an evolutionary track with one solar mass and $Z/Z_{\odot} = 1.0$ (see Fig. 4). The presented data and the plot symbols are the same as in Fig. 13.

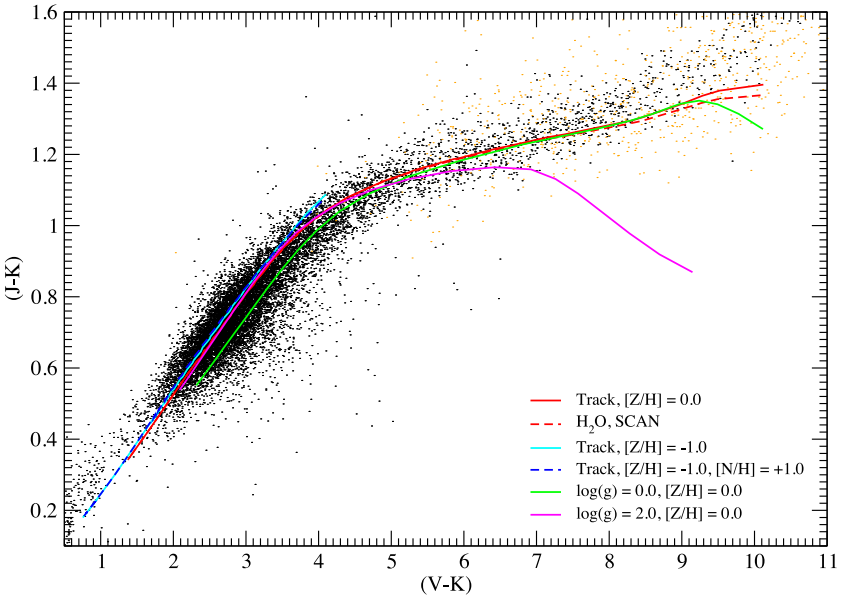

Figure 15. Two-colour diagram $(J - K)$ versus $(V - K)$ for different sequences of COMARCS atmospheres. Models placed along evolutionary tracks for stars with one solar mass and $Z/Z_{\odot} = 1.0$ (red solid line) as well as $Z/Z_{\odot} = 0.1$ (cyan solid line) are displayed (see Fig. 4). For the solar metallicity track, we show the effect of using the SCAN data for water (red dashed line) and for the metal-poor one the result of increasing nitrogen by a factor of 10 ([N/Z] = +1, blue dashed line). In addition, two sequences of models having solar mass and abundances with $\log(g\,[\mathrm{cm\,s^{-2}}]) = 0.0$ (green solid line, $T_{\rm eff} = 2600$–4800 K) and $\log(g\,[\mathrm{cm\,s^{-2}}]) = 2.0$ (magenta solid line, $T_{\rm eff} = 2600$–5000 K) are included. The dots represent cool giants in Baade's window (black) and Mira variables (orange) in the Galactic bulge.

theoretical and semi-empirical approaches. Especially for the coolest giants, the determination of the effective temperature is in general accompanied by considerable uncertainties. In addition to the issues mentioned in the previous paragraph, there are also problems concerning the measurement of the distances and radii of such extended objects. Thus, the differences between predicted and observed $(I - K)$ indices below 3300 K appearing in the second panel of the diagram are expected, while we find a quite good agreement of this colour for all warmer stars. The same applies to $(V - K)$, which is not shown here, since it behaves in a very similar way. We note that due to the divergent $(V - K)$ values of the coolest giants, the spacing of points in Fig. 13 is not equal at the low temperatures.

The predicted and observed $(J - K)$ indices in the upper panel of Fig. 14 agree in general quite well. However, the COMARCS models give above 4200 K slightly bluer and below 3200 K redder colours than the relations from Worthey & Lee (2011). This effect occurs also in the $(J - K)$ versus $(V - K)$ diagram in Fig. 13, where it is less pronounced. The solar values from Bessell et al. (1998), which are shown in the plot, can be found very close to our predicted sequence. It is possible that the shifts may be explained by small differences in the definition of the photometric filters, although Worthey & Lee (2011) use the same system in the near-infrared. Changes caused by a decreased microturbulent velocity are not sufficient to obtain the deviations.

The $(J - K)$ values as a function of effective temperature predicted by Bessell et al. (1998) in the range from 3600 to 5000 K for stars with $\log(g\,[\mathrm{cm\,s^{-2}}]) = 0.0$ and 2.0 are very similar to our COMARCS results with deviations below 0.025 mag in most of the cases. Somewhat larger differences appear only for the coolest models in the interval. In Worthey & Lee (2011), one can find plots where they compare a few of their relations concerning colours and bolometric corrections, which have been used here, to published theoretical work.

4.2 The Galactic bulge

4.2.1 Observational data

Simultaneous broad-band photometric measurements in the visual and the near-infrared for a whole population are only sparsely available in the literature. Therefore, we compiled data covering the Galactic bulge from different sources. Being dominated by cool giants located in the inner regions of the Milky Way, these observations can be compared to the modelling results as shown in Figs 15 and 16.

First, we adopted from public-domain surveys photometric observations in the direction of Baade's window, which is one of the low-extinction windows towards the centre of our galaxy (e.g. Dutra, Santiago & Bica 2002). For the visual filters V and I, we made use of the photometry obtained by the OGLE-II programme and downloaded the data of the Galactic bulge fields `bul_sc1` and `bul_sc45`, which cover Baade's window (cf. Udalski et al. 2002; Sumi 2004). Based on the exhaustive photometric time series of OGLE in I and an additional less extensive one in V, Udalski et al. (2002) provide mean magnitudes for all objects with values tied to the Landolt (1992) standards. Hence, no conversion to the Bessell system had to be applied. Dereddening was done with the help of extinction data derived by Sumi (2004) individually for the OGLE-II fields. The resulting colour–magnitude diagram for this rich population of about 530 000 stars can be seen in Fig. 16. The visual data were subsequently cross-correlated with near-infrared photometry of the 2MASS All-Sky Point Source Catalog (Skrutskie et al. 2006), which is made public by the NASA/IPAC Infrared Science Archive. Corresponding roughly to the above-mentioned OGLE fields in the Galactic bulge, we extracted photometric J, H and K_S measurements for an area of $\Delta\alpha \times \Delta\delta \approx 0.^{\circ}5 \times 1^{\circ}$. The correction for interstellar reddening was carried out according to Dutra et al. (2002) and Mathis (1990). The 2MASS data had to be

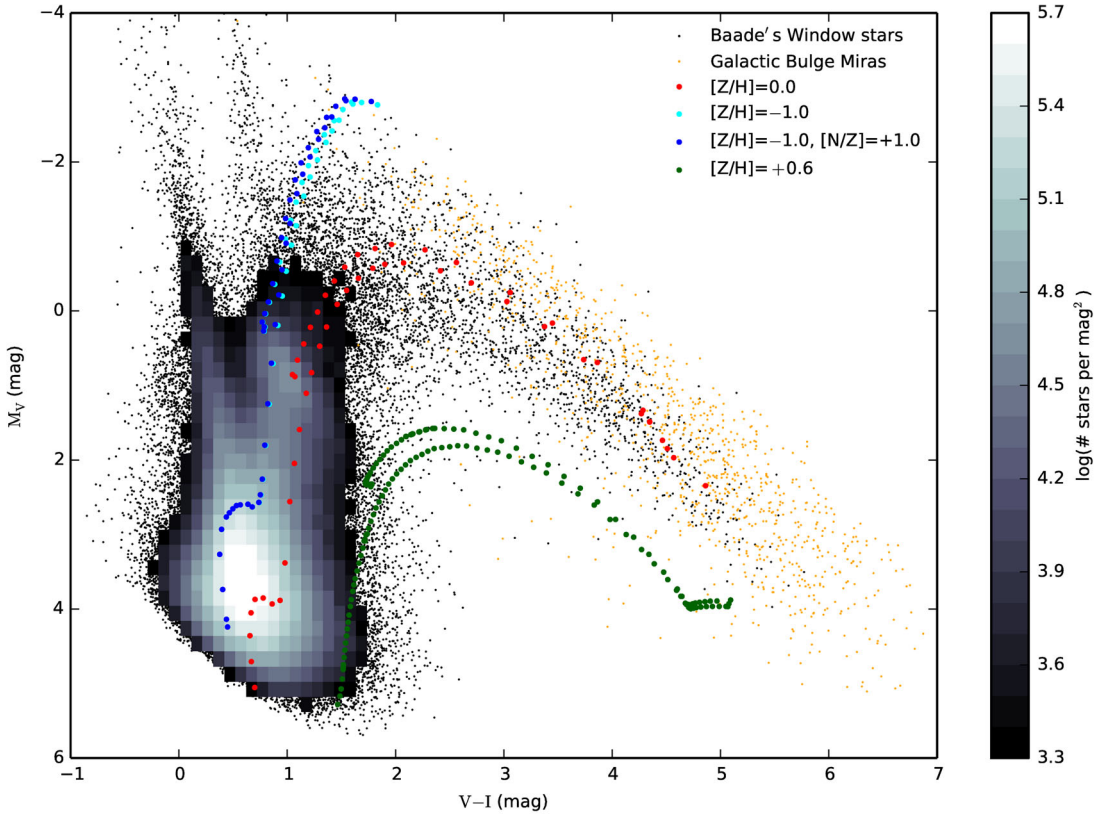

Figure 16. Colour–magnitude diagram M_V versus $(V - I)$ for COMARCS models placed along evolutionary tracks for stars with one solar mass and $Z/Z_{\odot} = 1.0$ (red circles) as well as $Z/Z_{\odot} = 0.1$ (cyan circles). For the metal-poor track, we show the effect of increasing nitrogen by a factor of 10 ([N/Z] = +1, blue circles). The dots represent cool giants in Baade's window (black) and Mira variables (orange) in the Galactic bulge. Due to the large number of objects in the first group, densities are plotted in the central region of their distribution. In addition, we show the points of a metal-rich evolutionary track with one solar mass and $Z/Z_{\odot} = 3.98$ (green circles), which were obtained from an interpolation in the COMARCS grid.

transformed to the Bessell system, chosen for the comparison in this work, using the relations provided by Carpenter (2001). As the 2MASS survey reaches not as deep as OGLE, the cross-correlation results in significantly less objects (about 14 000), which are shown in Fig. 15.

Secondly, we used for the comparison with our COMARCS models a sample of M-type Mira variables identified by Groenewegen & Blommaert (2005), who investigated the photometric variations appearing in the OGLE-II survey. These targets are not only located in Baade's window, but spread across the whole Galactic bulge. Groenewegen & Blommaert (2005) cross-correlated their list of objects with the 2MASS catalogue to get single epoch J, H and K_S photometry for the stars, which we will use here. The data have been dereddened adopting the interstellar extinction values for the various OGLE-II fields as derived by Matsunaga, Fukushi & Nakada (2005). For the conversion to magnitudes in the Bessell system, we applied again the equations of Carpenter (2001). In addition to the near-infrared photometry, Groenewegen (private communication) cross-correlated the selected Mira stars with the OGLE 'photometric maps' (Udalski et al. 2002) and provided mean V and I magnitudes, which we dereddened following Sumi (2004). This led to a sample of roughly 1000 objects that are also plotted in Figs 15 and 16.

When necessary, the apparent magnitudes of the bulge objects were transformed into absolute ones assuming a distance modulus of $(m - M) = 14.7$ mag for the centre of our galaxy (e.g. Vanhollebeke, Groenewegen & Girardi 2009).

4.2.2 *Models and the bulge population*

In Fig. 15, we present a two-colour diagram $(J - K)$ versus $(V - K)$, where we compare results obtained from different series of COMARCS atmospheres to measured values of the giants and Mira variables in the Galactic bulge. First, the plot includes two sequences of models placed along stellar evolution tracks for one solar mass with [Z/H] = 0 and −1, which are described in Section 2.2 and displayed in Fig. 4. The calculations having the metallicity of the Sun were already used before, when we discussed the relations of Worthey & Lee (2011). They produce colours, which are almost for the complete range covered by the diagram located in the centre of the distribution of the observed stars. Deviations appear mainly for the coolest effective temperatures, where the $(J - K)$ indices of the bulge objects tend to be higher. There exists also a sparsely populated red tail extending up to $(V - K) = 14$ and $(J - K) = 3$, which is not visible in the plot and far away from the shown COMARCS atmospheres. It contains mostly Mira variables. We have already noted that such cool giants can usually not be described by simple hydrostatic models, since they are dominated by pulsation, convection, mass-loss and dust formation. In addition, the connected temporal changes may create problems concerning the observed photometric values, if they were not taken at the same time. Very red $(V - K)$ and $(J - K)$ colours can also be produced by COMARCS atmospheres with a high C/O ratio between 0.8 and 1.0 (see Figs 9 and 11) or with a combination of an increased metallicity and a quite low effective temperature. The first of these scenarios

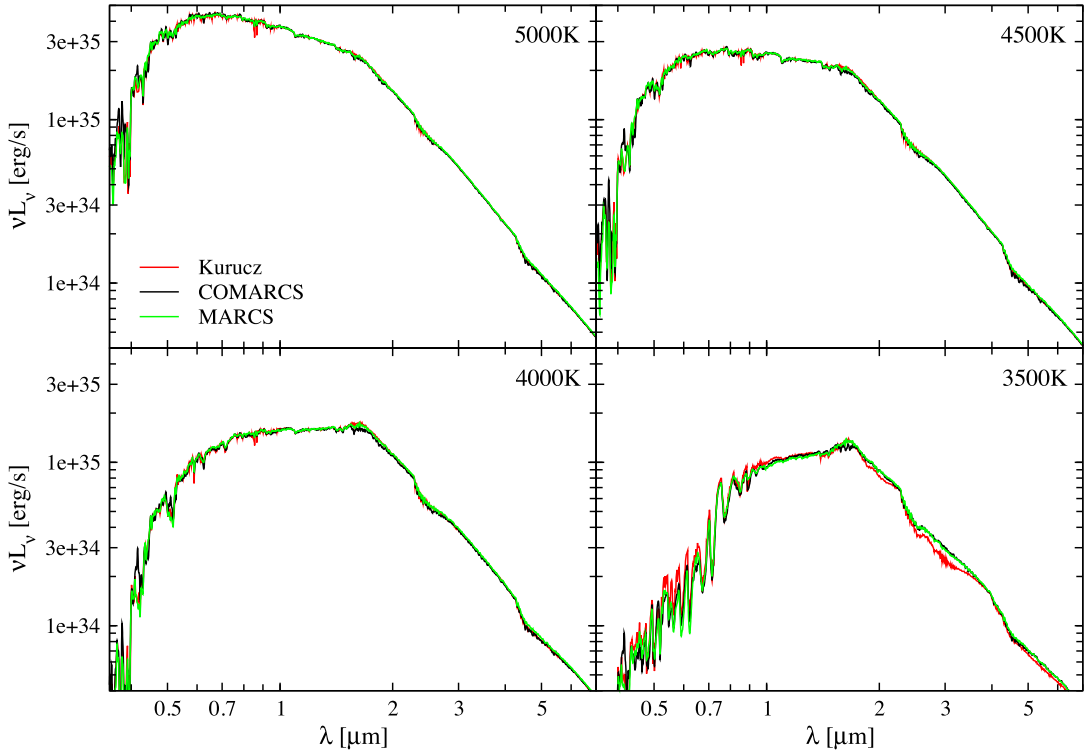

Figure 17. Spectra based on COMARCS models with $\log(g\,[\mathrm{cm\,s^{-2}}]) = 2.0$, $M/\mathrm{M}_\odot = 1.0$, solar abundances and four different effective temperatures (5000, 4500, 4000, 3500 K, black) are compared to published MARCS (green) and Kurucz (red) spectra corresponding to identical parameters. In the case of COMARCS and MARCS, the original opacity sampling resolution of the radiative transfer has been degraded to $R = 200$. The Kurucz spectra (opacity distribution function) are plotted without any modification resulting in a somewhat higher resolution of narrow features. Also the solar abundances used for the model grids differ a bit.

is not so probable, since we find no classic carbon stars in the Galactic bulge. The good agreement of the models placed along the [*Z*/H] = 0 track with the bulk of the observed giants confirms the result from the comparison with the relations of Worthey & Lee (2011) in Fig. 13, where we see only weak deviations.

For the stellar evolution track with [*Z*/H] = −1, we show an additional sequence of COMARCS atmospheres, where nitrogen was enhanced by a factor of 10. However, there is almost no difference between the series with [N/*Z*] = 0 and +1 in the diagram. One can see already in Figs 9 and 11 that the impact of this parameter on $(V - K)$ and $(J - K)$ remains quite small. Both low-metallicity sequences cover only the blue part of the plot. Due to the high effective temperatures of the corresponding stellar evolution track, they do not exceed values around 4.2 in $(V - K)$ and 1.1 in $(J - K)$.

In Fig. 15, we have also added some extra series of COMARCS atmospheres with solar abundances. For the cooler models located on the evolutionary track, a sequence is shown, which was obtained from spectra calculated using the SCAN line list for water as described in Section 2.1. One can see that the selection of the H_2O opacity has a small influence on the position in the diagram. The corresponding changes are not sufficient to decide which data source is better. In order to prove the importance of adopting the correct surface gravity, when synthetic photometry is derived from models, we have also included two effective temperature sequences with solar mass and a constant $\log(g\,[\mathrm{cm\,s^{-2}}])$ of 0.0 and +2.0. Both of them can only explain a part of the observed distribution of giants in the Galactic bulge.

In Fig. 16, we present a colour–magnitude diagram M_V versus $(V - I)$, where we compare again COMARCS atmospheres located on stellar evolution tracks for one solar mass with [*Z*/H] = 0 and −1 to giants in the Galactic bulge. Also the calculations with [N/*Z*] = +1 were included for the lower metallicity. The sequence of models having the chemical abundances of the Sun agrees quite well with the observed stars. It covers almost the complete colour range being always very close to the centre of their distribution. Only the reddest objects, which were usually classified as Mira variables, are not reached by the COMARCS atmospheres. As has already been discussed, such giants cannot be described by hydrostatic models. We may conclude that stars with a mass and metallicity similar to the solar values are typical for the investigated Galactic bulge population. Independent of the nitrogen abundance, which causes small changes in $(V - I)$, the sequence with [*Z*/H] = −1 covers only quite blue colours in the diagram. This is due to the high effective temperatures of the corresponding stellar evolution tracks. As one can see, the most luminous of these models are located in a region, where the density of observed stars is very low. They appear to be not so common in the studied bulge population.

In Fig. 16, we have also included the points of a metal-rich evolutionary track with one solar mass and [*Z*/H] = +0.6, which were obtained from an interpolation in the COMARCS grid as described in Section 4.3. The redder stars of this sequence are obviously as well not common in the investigated region of the bulge. Their low fluxes in the *V* filter can be explained by the fact that at higher [*Z*/H] the models having a given luminosity become in general cooler, while the depth of the TiO bands and many atomic lines increases even at a constant effective temperature. Using only the data shown in the plot, it is not possible to exclude the existence of a considerable population of evolved giants with a certain larger or smaller metallicity, since they may have a different mass (age) or

[O/Z]. This would require a more detailed study covering a variation of the two parameters.

4.3 Hydrostatic model atmospheres and stellar evolution

The bulk of the models presented in this paper can be used to define a three-dimensional grid with $T_{\rm eff}$, log (g) and [Z/H] as parameters. For the sake of transforming theoretical results obtained from COMARCS atmospheres into absolute magnitudes and colours, we make the interpolation first in the effective temperature versus surface gravity grids of the confining metallicity values. Then we interpolate in [Z/H]. A scheme identical to the one described in section 4.2 of Aringer et al. (2009) was applied.

The other parameters investigated in Section 3, which are C/O ratio, nitrogen abundance and stellar mass, have only been covered by sparser grids or even more limited sequences of models. However, they are demonstrated not to be as crucial as the main quantities. In order to consider their effect, we simply apply corrections to the photometric results obtained from the interpolation, which depend on temperature and surface gravity. For each of the involved parameters, this is done separately. It allows us to implement the phenomena discussed in Section 3, like the variation of the TiO bands at short wavelengths as a function of C/O ratio and mass or the changes caused by the CN features in warmer stars, in an approximated way. Needless to say that the current interpolation routine is preliminary and may be modified significantly as we expand the COMARCS grid.

The result of the interpolation is the bolometric corrections for any desired combination of stellar parameters, which may be computed for a wide variety of photometric systems. This allows us to convert the values tabulated in theoretical isochrones into magnitudes and colours corresponding to the photospheres, if we study populations of stars. For the warmer objects not covered by the COMARCS grid, we use other libraries, which are at the moment either the one from Castelli & Kurucz (2003) as in Marigo et al. (2008) or the PHOENIX BT-Settl data (Allard et al. 2012; Rajpurohit et al. 2013) as in Chen et al. (2014). In the transition region, which occurs in the effective temperature interval from 4000 to 5000 K, we make a linear interpolation between the input sets. One can see in Fig. 17 that in this range, different hydrostatic codes give very similar overall energy distributions. The plot shows low-resolution spectra based on COMARCS, MARCS (Gustafsson et al. 2008) and Kurucz (Castelli & Kurucz 2003) models with 5000, 4500, 4000 and 3500 K having $\log(g\,[\mathrm{cm\,s^{-2}}]) = 2.0$ and the mass as well as the abundances of the Sun. Considerable deviations, which are in general due to the use of varying opacity data, appear almost only for the coolest atmospheres. Thus, we expect in the region from 4000 to 5000 K a smooth transition between the photometric results from different libraries.

When necessary, we consider the effect of the circumstellar dust shells on the derived absolute magnitudes as described in Marigo et al. (2008). This procedure is currently being revised and improved (Nanni et al., in preparation). Theoretical isochrones computed using transformations taken from the presented data base are made available as an additional option in the CMD web interface http://stev.oapd.inaf.it/cmd.

5 CONCLUSIONS

We have presented a grid of hydrostatic COMARCS atmospheres covering mainly stars with effective temperatures up to 5000 K, which is intended to be used in combination with stellar evolution calculations. The corresponding $R = 10\,000$ opacity sampling and convolved $R = 200$ spectra as well as the bolometric corrections for a large number of photometric systems can be downloaded from http://starkey.astro.unipd.it/atm. Since the data base is continuously growing, there will be frequent upgrades of the online material in the future. For example, we recompute and extend the carbon star grid of Aringer et al. (2009) considering the improvements described in Section 2.1. Also the amount of available models for S giants should be increased using s-process element abundances predicted by the stellar evolution codes. We want to emphasize again that due to their statistical nature the high-resolution opacity sampling spectra must not be directly compared to observations.

Using the data currently available in the COMARCS grid, we have investigated the spectroscopic and photometric properties of K and M giants. The consequences of adopting different masses, C/O ratios and an increased nitrogen abundance are studied. In general, these quantities cause much smaller changes than the main stellar parameters effective temperature, surface gravity and overall metallicity. Nevertheless, in many cases they cannot be neglected depending on the wavelength ranges of the filters and spectra and on the type of the star. A good example is the phenomenon described in Section 3.2.2 that the intensity of the TiO bands grows with lower mass, while the molecular absorption in the mid- and far-infrared decreases. This happens only in extended giants with $\log(g\,[\mathrm{cm\,s^{-2}}]) \leq 0.0$ and changes the V, R and I fluxes. In addition, the depth of the TiO features depends on the C/O ratio, which also affects the lines of CO and water. However, in this case, the behaviour is more complex, since it varies with temperature. The trend appearing in the coolest models below about 3100 K that the TiO bands get stronger with higher C/O values at least partly reverses in the warmer ones. As one can see in Section 3.3, this is also reflected by the $(V - K)$ and $(V - I)$ indices. The consequences of an enhancement of s-process elements often connected to an increased C/O ratio are not discussed here, because we do not focus on S giants. A higher nitrogen abundance, which has no effect below 3200 K, changes mainly the atomic and CN features.

Models with variable masses, C/O ratios and nitrogen abundances are not available for all combinations of the basic stellar parameters. In addition, we have no calculations covering a simultaneous change of these quantities. Thus, their effect is included with correction terms applied to the interpolation results, when the COMARCS grid is used to determine the observable properties of stars. Those factors should be taken from COMARCS atmospheres having parameters as close as possible, since they may vary a lot with temperature or surface gravity. Therefore, it is desirable to compute further sequences of models differing in mass, C/O value and nitrogen abundance. Dense grids are at the moment only available for a changed C/O ratio.

When we compare the photometric results obtained from the COMARCS grid to observed relations and to data for the Galactic bulge, we get in general a good agreement. Considerable deviations appear only for the coolest stars with effective temperatures below about 3200 K at solar metallicity and for very red colours of Mira variables. This is expected, since such giants show strong pulsations and mass-loss and may be obscured by circumstellar dust. Due to their dynamical nature, those phenomena cannot be covered by hydrostatic calculations. In that case, grids of models, which take the mentioned processes into account, are needed (e.g. Eriksson et al. 2014; Bladh et al. 2015). For the combination with stellar evolution results, the influence of dust is often approximated with pure radiative transfer or more simple stationary wind computations.

We have also investigated the effect of using different opacity data for water, which create some deviations in the spectra of cool M giants. But the corresponding changes of the photometric properties studied here are not large enough to select a preferred line list, if one considers all other uncertainties appearing for such objects.

ACKNOWLEDGEMENTS

This work was mainly supported by the ERC Consolidator Grant funding scheme (*project STARKEY*, G.A. no. 615604). PM acknowledges support from Progetto di Ateneo 2012, University of Padova, ID: CPDA125588/12. Sincere thanks are given to M. A. T. Groenewegen and J. A. D. L. Blommaert who provided mean OGLE-VI magnitudes for the Galactic bulge Miras. This research has made use of the NASA/IPAC Infrared Science Archive, which is operated by the Jet Propulsion Laboratory, California Institute of Technology, under contract with the National Aeronautics and Space Administration. This publication makes use of data products from the Two Micron All Sky Survey, which is a joint project of the University of Massachusetts and the Infrared Processing and Analysis Center/California Institute of Technology funded by the National Aeronautics and Space Administration and the National Science Foundation. We thank Marco Dussin for helping us with the electronic publication of the data.

REFERENCES

Allard F., Homeier D., Freytag B., 2012, Phil. Trans. R. Soc. A, 370, 2765
Alvarez R., Jorissen A., Plez B., Gillet D., Fokin A., Dedecker M., 2001, A&A, 379, 305
Aringer B., 2000, PhD thesis, Univ. Vienna, Wien
Aringer B., Jørgensen U. G., Langhoff S. R., 1997, A&A, 323, 202
Aringer B., Kerschbaum F., Jørgensen U. G., 2002, A&A, 395, 915
Aringer B., Girardi L., Nowotny W., Marigo P., Lederer M. T., 2009, A&A, 503, 913
Barber R. J., Tennyson J., Harris G. J., Tolchenov R. N., 2006, MNRAS, 368, 1087
Bauschlicher C. W., Ram R. S., Bernath P. F., Parsons C. G., Galehouse D., 2001, J. Chem. Phys., 115, 1312
Bell R. A., Gustafsson B., 1989, MNRAS, 236, 653
Bensby T. et al., 2010, A&A, 512, A41
Bensby T. et al., 2011, A&A, 533, A134
Bessell M. S., 1990, PASP, 102, 1181
Bessell M. S., Brett J. M., 1988, PASP, 100, 1134
Bessell M. S., Brett J. M., Wood P. R., Scholz M., 1989, A&AS, 77, 1
Bessell M. S., Castelli F., Plez B., 1998, A&A, 333, 231
Bladh S., Höfner S., Aringer B., Eriksson K., 2015, A&A, 575, A105
Bohlin R. C., 2007, in Sterken C., ed., ASP Conf. Ser. Vol. 364, The Future of Photometric, Spectrophotometric and Polarimetric Standardization. Astron. Soc. Pac., San Francisco, p. 315
Bolatto A. D. et al., 2007, ApJ, 655, 212
Borysow A., 2002, A&A, 390, 779
Borysow A., Jørgensen U. G., Fu Y., 2001, J. Quant. Spectrosc. Radiat. Transfer, 68, 235
Boyer M. L. et al., 2013, ApJ, 774, 83
Bressan A., Marigo P., Girardi L., Salasnich B., Dal Cero C., Rubele S., Nanni A., 2012, MNRAS, 427, 127
Burrows A., Dulick M., Bauschlicher C. W., Jr, Bernath P. F., Ram R. S., Sharp C. M., Milsom J. A., 2005, ApJ, 624, 988
Busso M., Gallino R., Wasserburg G. J., 1999, ARA&A, 37, 239
Caffau E., Ludwig H.-G., Steffen M., 2009a, Mem. Soc. Astron. Ital., 80, 643
Caffau E., Maiorca E., Bonifacio P., Faraggiana R., Steffen M., Ludwig H.-G., Kamp I., Busso M., 2009b, A&A, 498, 877
Carpenter J. M., 2001, AJ, 121, 2851
Castelli F., Kurucz R. L., 2003, in Piskunov N., Weiss W. W., Gray D. F., eds, Proc. IAU Symp. 210, Modelling of Stellar Atmospheres. Astron. Soc. Pac., San Francisco, p. 20
Chandra S., Kegel W. H., Le Roy R. J., Hertenstein T., 1995, A&AS, 114, 175
Chen Y., Girardi L., Bressan A., Marigo P., Barbieri M., Kong X., 2014, MNRAS, 444, 2525
Cioni M.-R. L. et al., 2011, A&A, 527, A116
Clem J. L., VandenBerg D. A., Grundahl F., Bell R. A., 2004, AJ, 127, 1227
Cristallo S., Straniero O., Lederer M. T., Aringer B., 2007, ApJ, 667, 489
Cristallo S. et al., 2011, ApJS, 197, 17
Dalcanton J. J. et al., 2012a, ApJS, 198, 6
Dalcanton J. J. et al., 2012b, ApJS, 200, 18
Dutra C. M., Santiago B. X., Bica E., 2002, A&A, 381, 219
Eriksson K., Nowotny W., Höfner S., Aringer B., Wachter A., 2014, A&A, 566, A95
Fluks M. A., Plez B., The P. S., de Winter D., Westerlund B. E., Steenman H. C., 1994, A&AS, 105, 311
Gautschy-Loidl R., Höfner S., Jørgensen U. G., Hron J., 2004, A&A, 422, 289
Girardi L., Bertelli G., Bressan A., Chiosi C., Groenewegen M. A. T., Marigo P., Salasnich B., Weiss A., 2002, A&A, 391, 195
Groenewegen M. A. T., Blommaert J. A. D. L., 2005, A&A, 443, 143
Gustafsson B., Bell R. A., 1979, A&A, 74, 313
Gustafsson M., Frommhold L., 2001, ApJ, 546, 1168
Gustafsson M., Frommhold L., 2003, A&A, 400, 1161
Gustafsson B., Bell R. A., Eriksson K., Nordlund A., 1975, A&A, 42, 407
Gustafsson B., Edvardsson B., Eriksson K., Jørgensen U. G., Nordlund Å., Plez B., 2008, A&A, 486, 951
Henyey L., Vardya M. S., Bodenheimer P., 1965, ApJ, 142, 841
Houdashelt M. L., Bell R. A., Sweigart A. V., Wing R. F., 2000, AJ, 119, 1424
Husser T.-O., Wende-von Berg S., Dreizler S., Homeier D., Reiners A., Barman T., Hauschildt P. H., 2013, A&A, 553, A6
Ita Y. et al., 2008, PASJ, 60, 435
Jørgensen U. G., 1994, A&A, 284, 179
Jørgensen U. G., 1997, in van Dishoeck E. F., ed., Proc. IAU Symp. 178, Molecules in Astrophysics: Probes and Processes. Kluwer, Dordrecht, p. 441
Jørgensen U. G., Johnson H. R., Nordlund A., 1992, A&A, 261, 263
Jørgensen U. G., Hammer D., Borysow A., Falkesgaard J., 2000, A&A, 361, 283
Jørgensen U. G., Jensen P., Sørensen G. O., Aringer B., 2001, A&A, 372, 249
Kato D. et al., 2007, PASJ, 59, 615
Landolt A. U., 1992, AJ, 104, 372
Lançon A., Wood P. R., 2000, A&AS, 146, 217
Lançon A., Hauschildt P. H., Ladjal D., Mouhcine M., 2007, A&A, 468, 205
Lebzelter T., Nowotny W., Hinkle K. H., Höfner S., Aringer B., 2014, A&A, 567, A143
Lederer M. T., Aringer B., 2009, A&A, 494, 403
Levesque E. M., Massey P., Olsen K. A. G., Plez B., Josselin E., Maeder A., Meynet G., 2005, ApJ, 628, 973
Marigo P., Girardi L., Bressan A., Groenewegen M. A. T., Silva L., Granato G. L., 2008, A&A, 482, 883
Marigo P., Bressan A., Nanni A., Girardi L., Pumo M. L., 2013, MNRAS, 434, 488
Mathis J. S., 1990, ARA&A, 28, 37
Matsunaga N., Fukushi H., Nakada Y., 2005, MNRAS, 364, 117
Matsuura M., Yamamura I., Cami J., Onaka T., Murakami H., 2002, A&A, 383, 972
Meixner M. et al., 2006, AJ, 132, 2268
Nikutta R., Hunt-Walker N., Nenkova M., Ivezić Ž., Elitzur M., 2014, MNRAS, 442, 3361
Nowotny W., Höfner S., Aringer B., 2010, A&A, 514, A35
Nowotny W., Aringer B., Höfner S., Lederer M. T., 2011, A&A, 529, A129

Nowotny W., Gail H.-P., Posch T., Aringer B., 2015, in Kerschbaum F., Wing R. F., Hron J., eds, ASP Conf. Ser. Vol. 497, Why Galaxies Care about AGB Stars III: A Closer Look in Space and Time. Astron. Soc. Pac., San Francisco, p. 397
Partridge H., Schwenke D. W., 1997, J. Chem. Phys., 106, 4618
Plez B., 1998, A&A, 337, 495
Plez B., Brett J. M., Nordlund A., 1992, A&A, 256, 551
Rajpurohit A. S., Reylé C., Allard F., Homeier D., Schultheis M., Bessell M. S., Robin A. C., 2013, A&A, 556, A15
Rayner J. T., Cushing M. C., Vacca W. D., 2009, ApJS, 185, 289
Rothman L. S. et al., 2005, J. Quant. Spectrosc. Radiat. Transfer, 96, 139
Rothman L. S. et al., 2009, J. Quant. Spectrosc. Radiat. Transfer, 110, 533
Rothman L. S. et al., 2010, J. Quant. Spectrosc. Radiat. Transfer, 111, 2139
Sauval A. J., Tatum J. B., 1984, ApJS, 56, 193
Schwenke D. W., 1998, Faraday Discuss., 109, 321
Shayesteh A., Henderson R. D. E., Le Roy R. J., Bernath P. F., 2007, J. Phys. Chem. A, 111, 12495
Skrutskie M. F. et al., 2006, AJ, 131, 1163
Skory S., Weck P. F., Stancil P. C., Kirby K., 2003, ApJS, 148, 599
Smith V. V., Lambert D. L., 1985, ApJ, 294, 326
Smith V. V., Lambert D. L., 1990, ApJS, 72, 387
Sumi T., 2004, MNRAS, 349, 193
Udalski A. et al., 2002, Acta Astron., 52, 217
Uttenthaler S., Blommaert J. A. D. L., Wood P. R., Lebzelter T., Aringer B., Schultheis M., Ryde N., 2015, MNRAS, 451, 1750
van Eck S. et al., 2011, in Kerschbaum F., Lebzelter T., Wing R. F., eds, ASP Conf. Ser. Vol. 445, Why Galaxies Care about AGB Stars II: Shining Examples and Common Inhabitants. Astron. Soc. Pac., San Francisco, p. 71
VandenBerg D. A., Clem J. L., 2003, AJ, 126, 778
Vanhollebeke E., Groenewegen M. A. T., Girardi L., 2009, A&A, 498, 95
Weck P. F., Stancil P. C., Kirby K., 2003a, J. Chem. Phys., 118, 9997
Weck P. F., Schweitzer A., Stancil P. C., Hauschildt P. H., Kirby K., 2003b, ApJ, 582, 1059
Windsteig W., Dorfi E. A., Hoefner S., Hron J., Kerschbaum F., 1997, A&A, 324, 617
Worthey G., Lee H.-c., 2011, ApJS, 193, 1

APPENDIX A: THE CURRENT COMARCS GRID

In Table A1, we list the various opacity sets that are currently available within the COMARCS grid. Each of them is defined by a certain selection of elemental abundances, microturbulent velocity and input data for the absorption and may include model atmospheres with different effective temperature, surface gravity or mass. A description of the corresponding calculations can be found in Section 2. We want to emphasize that the information in Table A1 represents only a snapshot at the time when this paper was produced, since additional models will be computed in the future. Thus, we do not give a complete list of available COMARCS atmospheres here. The corresponding data may be obtained from http://starkey.astro.unipd.it/atm.

The main parameters of the opacity sets are the overall metallicity [*Z*/H] as described in Section 2.2, the abundance of oxygen [O/H], the C/O ratio and the microturbulent velocity. We have also varied the amount of some key elements like N or Zr. [alp/H] = bulge in Table A1 stands for the α abundances from Bensby et al. (2010, 2011). In addition, we have computed dwarf models without CIA. The quantities [*Z*/H], [O/H] and C/O are given in the listings and files of the data base by the number density of iron, oxygen and carbon relative to hydrogen $\log(\varepsilon_{\mathrm{Fe,O,C}}/\varepsilon_{\mathrm{H}}) + 12$.

Table A1. The opacity sets available in the COMARCS grid. They are mainly characterized by the abundances of the bulk of metals [*Z*/H] and of oxygen [O/H] relative to the solar values as well as by the C/O ratio and microturbulent velocity (ξ). Additional parameters are listed in an extra column. We have also included information about the lowest and highest effective temperature ($T_{\mathrm{min,max}}$) and $\log(g\,[\mathrm{cm\,s^{-2}}])$ covered by the models of a set. The status tells how many COMARCS atmospheres are available: grd = big grid, grh = small limited grid, seq = one or more sequences, not = no models, only opacity tables.

[*Z*/H]	[O/H]	C/O	ξ (km s^{-1})	Other parameters	T_{min} (K)	T_{max} (K)	$\log(g)_{\mathrm{min}}$	$\log(g)_{\mathrm{max}}$	Status
0.00	0.00	0.550	2.5		2600	5940	− 1.00	5.32	grd
0.00	0.00	0.550	2.5	BT2 water list					not
0.00	0.00	0.550	2.5	no CIA	2600	5000	5.00	5.00	seq
0.00	0.00	0.550	1.5		2600	5800	0.00	5.00	seq
0.00	0.00	0.550	5.0		2600	5000	5.00	5.00	seq
0.00	0.00	0.550	2.5	[N/Z] = +1.00	2600	5000	0.00	2.00	seq
0.00	0.00	0.300	2.5		2600	4600	− 0.95	2.50	grd
0.00	0.00	0.700	2.5		2600	4000	− 0.95	2.00	grd
0.00	0.00	0.800	2.5		2600	3500	− 0.95	0.00	grd
0.00	0.00	0.900	2.5		2600	3500	− 1.00	0.00	grd
0.00	0.00	0.950	2.5		2600	3500	− 0.95	0.00	grd
0.00	0.00	0.970	2.5		2600	4000	0.00	0.00	seq
0.00	0.00	0.970	2.5	[Y/Z] & [Zr/Z] = +1.5	2500	4000	− 1.00	2.00	grd
− 0.41	− 0.41	0.550	2.5						not
− 0.41	− 0.64	0.374	2.5	[O/Z] = −0.23, [N/Z] = +1.32					not
− 0.41	− 0.63	0.596	2.5	[O/Z] = −0.23, [N/Z] = +1.32					not
− 0.41	− 0.63	0.841	2.5	[O/Z] = −0.23, [N/Z] = +1.32					not
− 0.50	− 0.50	0.550	2.5		2600	5000	− 1.00	5.00	grd
− 0.50	0.00	0.275	2.5	[O/Z] = +0.5, [alp/H] = bulge	2600	5000	− 0.95	5.00	grd
− 0.70	− 0.70	0.550	2.5		2600	4500	0.00	2.50	grd
− 0.70	− 0.70	0.250	2.5		2600	4500	0.00	2.50	grd
− 1.00	− 1.00	0.550	2.5		2600	7171	− 1.00	5.00	grd
− 1.00	− 1.00	0.550	2.5	no CIA	2800	4000	5.00	5.00	seq
− 1.00	− 1.00	0.550	2.5	[N/Z] = +1.00	2600	7171	0.00	4.53	seq
− 1.49	− 1.49	0.550	2.5		2800	5000	4.50	5.00	seq
− 1.50	− 1.50	0.550	2.5		2600	5000	− 0.95	5.00	grd

Table A1 – *continued*

[Z/H]	[O/H]	C/O	ξ (km s^{-1})	Other parameters	$T_{\rm min}$ (K)	$T_{\rm max}$ (K)	log(g)$_{\rm min}$	log(g)$_{\rm max}$	Status
−2.00	−2.00	0.550	2.5		2600	5000	−1.00	5.00	grd
0.50	0.50	0.550	2.5		2600	5000	−0.90	5.00	grd
1.00	1.00	0.550	2.5		2600	5000	−0.65	5.00	grd
1.50	1.50	0.550	2.5						not
0.00	0.00	1.010	2.5		2600	4000	−0.95	2.00	grd
0.00	0.00	1.010	2.5	[Y/Z] & [Zr/Z] = +1.0	2600	4000	0.00	0.00	seq
0.00	0.00	1.050	2.5		2500	4000	−1.00	2.00	grd
0.00	0.00	1.100	2.5		2600	4500	−0.95	2.00	grd
0.00	0.00	1.400	2.5		2600	4000	−0.95	0.00	seq
0.00	0.00	2.000	2.5		2600	4200	0.00	0.00	seq
0.00	0.00	1.050	2.5	[N/Z] = −1.0	2600	4000	0.00	0.00	seq
0.00	0.00	1.050	2.5	[N/Z] = −5.0	2600	4000	0.00	0.00	seq
0.00	0.00	1.400	2.5	[N/Z] = −1.0					not
0.00	0.00	1.400	2.5	[N/Z] = −5.0					not
−0.50	−0.50	1.050	2.5		2600	4000	0.00	0.00	seq
−0.50	−0.50	1.100	2.5		2500	4000	0.00	0.00	seq
−0.50	−0.50	1.400	2.5		2500	4000	0.00	0.00	seq
−0.50	−0.50	2.000	2.5		2500	4000	0.00	0.00	seq
−0.50	−0.50	4.000	2.5		2500	4000	0.00	0.00	seq
−0.50	−0.50	8.000	2.5		2500	4000	0.00	0.00	seq
−1.00	−1.00	1.100	2.5						not
−1.00	−1.00	1.400	2.5						not
−1.00	−1.00	2.000	2.5						not
−1.00	−1.00	4.000	2.5						not
−1.00	−1.00	8.000	2.5						not
−2.00	−2.00	1.400	2.5		3600	4200	0.00	2.50	grh
−2.00	−2.00	2.000	2.5		3600	4200	0.00	2.50	grh
−2.00	−2.00	6.000	2.5		3600	4200	0.00	2.50	grh
−2.00	−2.00	10.000	2.5		3800	4200	0.00	2.50	grh
−2.00	−1.50	10.000	2.5	[C/Z] & [N/Z] & [O/Z] = +0.5	3600	4200	0.50	2.50	grh

APPENDIX B: THE EXCESS OF FREE OXYGEN

Since in the cooler regions of an M star atmosphere, most of the carbon atoms form CO molecules, only the remaining amount of oxygen can be used to create other species like TiO, VO, H_2O or SiO, which represent important absorbers. Thus, the excess (O−C) given by $\log((\varepsilon_{\rm O} - \varepsilon_{\rm C})/\varepsilon_{\rm H}) + 12$ may dominate the overall opacity, if the abundances of C and O are changed. In order to investigate the effect of this quantity, we have calculated COMARCS models with [O/Z] increased to +1 keeping the (O−C) value of the Sun constant at 8.455. For the adopted solar metallicity this results in a C/O ratio of 0.955, instead of 0.55 at [O/Z] = 0. A comparison of spectra for giants with 2800 and 3600 K having normal and enhanced oxygen abundances is shown in Fig. B1.

For the cooler effective temperature, the spectra with [O/Z] = 0 and +1 are very similar, which is also true for the atmospheric structures. Differences appear mainly in the regions of the CO bands with the largest changes for the ground state, because the amount of this species increases at higher oxygen abundances. As expected, the absorption produced by the other molecules shows almost no variation, if (O−C) remains constant. For the hotter models, the situation is more complex. In addition to the CO bands, which become again deeper at higher [O/Z], several spectral features and the atmospheric structures change moderately. Even if the abundances of important metals like Ti or V are kept constant, (O−C) is in contrast to the cooler giants being not the only crucial parameter. This may be explained by the fact that in warmer stars the relative contribution of CO to the total opacity is larger and a significant fraction of the carbon atoms can form CN or CH.

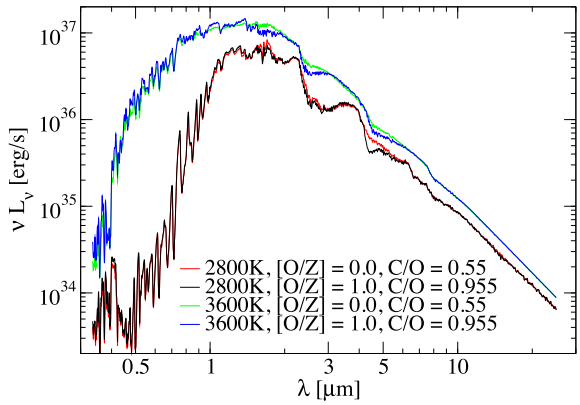

Figure B1. Spectra based on COMARCS models with $T_{\rm eff}$ = 2800 or 3600 K, log(g [cm s^{-2}]) = 0.0, one solar mass and solar metallicity. The effect of changing [O/Z] from 0 to +1 at a constant (O−C) of 8.455 is shown.

This paper has been typeset from a TEX/LATEX file prepared by the author.